CANCER

Ribonucleotide reductase regulatory subunit M2 drives glioblastoma TMZ resistance through modulation of dNTP production

Ella N. Perrault[1], Jack M. Shireman[1], Eunus S. Ali[2], Peiyu Lin[1], Isabelle Preddy[1], Cheol Park[1], Shreya Budhiraja[1], Shivani Baisiwala[1], Karan Dixit[3], C. David James[1,4], Dieter H Heiland[5,6,7,8], Issam Ben-Sahra[2], Sebastian Pott[9], Anindita Basu[9], Jason Miska[1,3], Atique U. Ahmed[1,3]*

During therapy, adaptations driven by cellular plasticity are partly responsible for driving the inevitable recurrence of glioblastoma (GBM). To investigate plasticity-induced adaptation during standard-of-care chemotherapy temozolomide (TMZ), we performed in vivo single-cell RNA sequencing in patient-derived xenograft (PDX) tumors of GBM before, during, and after therapy. Comparing single-cell transcriptomic patterns identified distinct cellular populations present during TMZ therapy. Of interest was the increased expression of ribonucleotide reductase regulatory subunit M2 (*RRM2*), which we found to regulate dGTP and dCTP production vital for DNA damage response during TMZ therapy. Furthermore, multidimensional modeling of spatially resolved transcriptomic and metabolomic analysis in patients' tissues revealed strong correlations between *RRM2* and dGTP. This supports our data that RRM2 regulates the demand for specific dNTPs during therapy. In addition, treatment with the RRM2 inhibitor 3-AP (Triapine) enhances the efficacy of TMZ therapy in PDX models. We present a previously unidentified understanding of chemoresistance through critical RRM2-mediated nucleotide production.

INTRODUCTION

Cellular carcinogenesis can be described as an evolutionary process (*1*–*5*). Subsequent to initial tumor development, therapy-associated selection pressures can alter tumor cell fate states that survive therapeutics to become the dominant and resistant population (*6*–*8*). Glioblastoma (GBM), the most aggressive primary adult brain tumor, typifies the process of cellular adaptation to therapeutic intervention, ultimately resulting in resistance and fatal recurrence (*9*, *10*). Because of a lack of access to GBM tissue during the standard-of-care chemo- and radiotherapy (*11*, *12*), research has predominantly focused on investigating GBM before and/or after therapeutic intervention. However, focusing solely on pre- and post-therapy GBM is insufficient, as tumor evolution is a dynamic process (*1*–*10*). We hypothesize that the population(s) of GBM cells that drive intratumoral adaptations, support therapeutic resistance, and promote tumor recurrence arises during therapy and remains largely unknown.

Establishing a model of GBM to capture the evolutionary dynamics of GBM during therapy would help identify therapeutically actionable adaptation mechanisms (*7*, *13*–*16*). To investigate this, our laboratory has performed in vivo single-cell RNA sequencing (scRNA-seq) analysis of patient-derived xenograft (PDX) tumors, established in the brains of athymic mice, and isolated before, during, and after treatment with standard-of-care chemotherapy temozolomide (TMZ), which is used in treating all newly diagnosed GBM (*9*–*11*).

By comparing single-cell transcription expression patterns of tumors before, during, and after therapy, we identified unique cellular populations present in tumors undergoing TMZ treatment. We combined these data with an analysis of multidimensional spatially resolved transcriptomic data of 16 primary GBM patients' tissue. Our analyses show a previously unidentified role of ribonucleotide reductase (RNR) family genes in promoting resistance to TMZ. Classically, the β subunit of RNR, RRM2, or its isoform RRM2B, forms a complex with the α subunit RRM1 to create an RNR enzyme, which mediates deoxynucleotide triphosphate (dNTP) production (*17*). Our single-cell data reveal a compelling relationship between RNR subunits and their dependency on therapeutic progression. More specifically, the results of our study suggest that GBM cells increase *RRM2* subunit expression via epigenetic regulation during TMZ therapy and adapt to TMZ-induced DNA damage by producing specific dNTPs. In addition, we find that inhibition of RRM2 activity using second-generation inhibitor 3-AP (Triapine), a drug in several late-phase clinical studies (*18*), significantly increases the antitumor activity of TMZ in vivo, suggesting an opportunity for delaying recurrence. Overall, our data indicate a unique role of RRM2-mediated dNTP metabolism in adapting to therapeutic stress and identify RRM2 as a therapeutic target for improving treatment outcomes for GBM patients.

[1]Department of Neurological Surgery, Feinberg School of Medicine, Northwestern University, Chicago, IL, USA. [2]Department of Biochemistry and Molecular Genetics, Feinberg School of Medicine, Northwestern University, Chicago, IL, USA. [3]Department of Neurology, Feinberg School of Medicine, Northwestern University, Chicago, IL, USA. [4]Northwestern Medicine Malnati Brain Tumor Institute of the Lurie Comprehensive Cancer Center, Feinberg School of Medicine, Northwestern University, Chicago, IL, USA. [5]Microenvironment and Immunology Research Laboratory, Medical-Center, University of Freiburg, Freiburg, Germany. [6]Department of Neurosurgery, Medical-Center, University of Freiburg, Freiburg, Germany. [7]Faculty of Medicine, University of Freiburg, Freiburg, Germany. [8]German Cancer Consortium (DKTK), partner site Freiburg, Freiburg, Germany. [9]Section of Genetic Medicine, Department of Medicine, University of Chicago, Chicago, IL, USA.
*Corresponding author. Email: atique.ahmed@northwestern.edu

RESULTS

scRNA-seq analysis identifies uniquely expressed genes during TMZ therapy

To investigate TMZ treatment–associated changes in GBM, we used an orthotopic PDX model. Mice were treated with vehicle control [dimethyl sulfoxide (DMSO)], or TMZ 7 days after tumor implantation, for five subsequent days. The TMZ-treated mice were euthanized either after 2 days of TMZ therapy, thus during therapy, or following tumor recurrence. Intracranial tumors were extracted, and single-cell suspension was analyzed by DropSeq analysis (fig. S1A). Seurat v3.0 custom pipeline was used to distinguish human tumor cells from mouse cells transcriptomes. Using Seurat and principal components analysis (PCA), we identified 20 principal components (PCs) that were fed into an algorithm and generated 15 clusters to distinguish tumor transcriptomes with respect to treatment received (Fig. 1A and fig. S1B). These 15 clusters were analyzed for the total number of cells in each cluster, the percentage of cells in each condition, and the cell signaling pathway most representative of that cluster using the NCI-Nature database (Fig. 1, B and C) (*19*).

Clusters 0, 6, and 11 proved especially informative for identifying cellular subpopulations that increased in tumors during TMZ therapy. For example, 87.92% of cells from tumors "during therapy" were in cluster 11, whereas cells from "no therapy" and "post-therapy recurrent" tumors had 6.52 and 5.56% of cells in cluster 11, respectively.

We found a condition-specific pattern of distribution in our data in which cells isolated during therapy were uniquely clustered because of their transcriptome profile, compared to cells analyzed in the no therapy or post-therapy recurrent GBM conditions, which have some overlap (Fig. 1D and fig. S1C). There was limited influence because of cell cycle states on the distribution of cells based on their transcriptional signatures in our data, regardless of their condition (Fig. 1E). Moreover, during TMZ therapy, the cells were distributed evenly within separate phases of the cell cycle, with 38.14% of cells in the G_1 phase, 38.78% in the S phase, and 23.1% in the G_2-M phase.

We next applied Gene Set Enrichment Analysis (GSEA) to identify cell populations that were relatively stable across treatments, in which we saw cell type marker expression to be consistent across conditions (fig. S1, D to F). We also analyzed glioma stem-like cell (GSC) transcriptional signatures (Fig. 1F and fig. S1G). Results indicated that GSC signature mean expression significantly increased during therapy compared to post-therapy recurrent ($P = 0.001$) with elevated Notch signaling ($P = 0.04$), a key signaling hub that has been reported to promote the GSC niche (fig. S1H) (*20*–*22*).

When identifying oncogenic markers present in our data, we saw the expression of DNA repair markers and resistance markers to be significantly enriched during therapy compared to no therapy ($P = 9.70 \times 10^{-08}$) and post-therapy recurrent ($P = 9.54 \times 10^{-08}$) (Fig. 1G and fig. S1, I and J).

Pseudotime analysis allows us to analyze the one-dimensional view of a single time point extracted from scRNA-seq to understand how cells evolve along their individual paths and behave in the single-cell transcriptomic analysis (*23*, *24*). Since raw read counts cannot be compared significantly, we instead use read counts to create trajectories that allow us to assume the underlying developmental changes of cells and establish expression patterns. We used the calculated cells' pseudotimes to map the DNA repair and resistance gene expression trajectories in our data. We see gene set expression increasing uniformly along pseudotime, indicating that as cells become more genetically distinct, they will gain expression of these gene sets during TMZ therapy (fig. S1K).

To compare the difference in clinically relevant transcriptional subtypes of GBM, proposed by Verhaak *et al.* (*25*), we applied pseudotime analysis of Verhaak classical, mesenchymal, and proneural GBM subtypes, as well as the GSC cellular state. This analysis revealed that, compared to no therapy and post-therapy recurrent signatures of GBM, cells up-regulated during therapy uniformly increase in their expression of molecular subtypes as they progress along pseudotime (fig. S1L).

We then examined how oncogenic gene sets are globally distributed in our scRNA-seq data (fig. S2A). Analysis of oncogenic gene sets elevated during therapy, such as gene sets associated with *KRAS* and *ALK* signaling, is highly correlated with a stress response that could be activated by TMZ treatment (fig. S2, B and C). In addition, Monocle3 trajectory mapping predicts increasing KRAS and ALK gene set expression in cells receiving sustained TMZ therapy (fig. S2D). These scRNA-seq results are consistent with immunohistochemical results showing that CLSPN and DLX6, of the ALK gene set, are up-regulated in tumors during therapy compared to no therapy ($P < 0.01$) and post-therapy recurrent GBM ($P < 0.01$) (fig. S2, E to G).

The poor clinical outcomes of GBM can be largely attributed to intrinsic intratumoral heterogeneity, which can be partially understood through transcriptional spatial heterogeneity (*26*–*28*). Spatial genomic analysis conserves the transcriptional spatial heterogeneity of specific tumor regions, enhancing our understanding of the tumor as a whole (*29*). Thus, to identify the clinical significance of our scRNA-seq signatures, we also wanted to determine whether the gene signatures from our scRNA-seq in vivo PDX model were present in GBM human tissue. Therefore, unique gene signatures (top 30 genes) from the scRNA-seq states of no therapy, during therapy, and post-therapy recurrent were spatially mapped to primary GBM tissue (fig. S3A).

We used a multidimensional approach to integrate 16 GBM patients' tissues by spatially resolved RNA sequencing (stRNA-seq) analysis, thereby investigating the spatial distribution of our in vivo single-cell molecular signatures from different time points during TMZ therapy (*30*). We identified spatial correlations between the scRNA-seq signatures and GO (Gene Ontology) gene sets in primary GBM tissue (Fig. 1H). Point size and color indicate the weight of spatial correlation between comparisons. In our analysis, no therapy transcriptional signatures are localized to regions of the tumor that are likewise enriched for transcriptional proneural subtype markers, which is expected as the PDX line, GBM43, used in our experiments was initially identified as Verhaak proneural (*31*). However, the during therapy signature switches to being spatially correlated with transcriptional classical subtype markers. Ultimately, the distinct correlations shown between no therapy/proneural markers and during therapy/classical markers seem to converge in the post-therapy recurrent signature, which correlates strongly with both proneural and classical subtype markers.

The contrast between no therapy and post-therapy recurrent GBM is also indicated by analyzing the correlation between scRNA-seq signatures and markers of neuronal development. While the no therapy signature is spatially correlated with

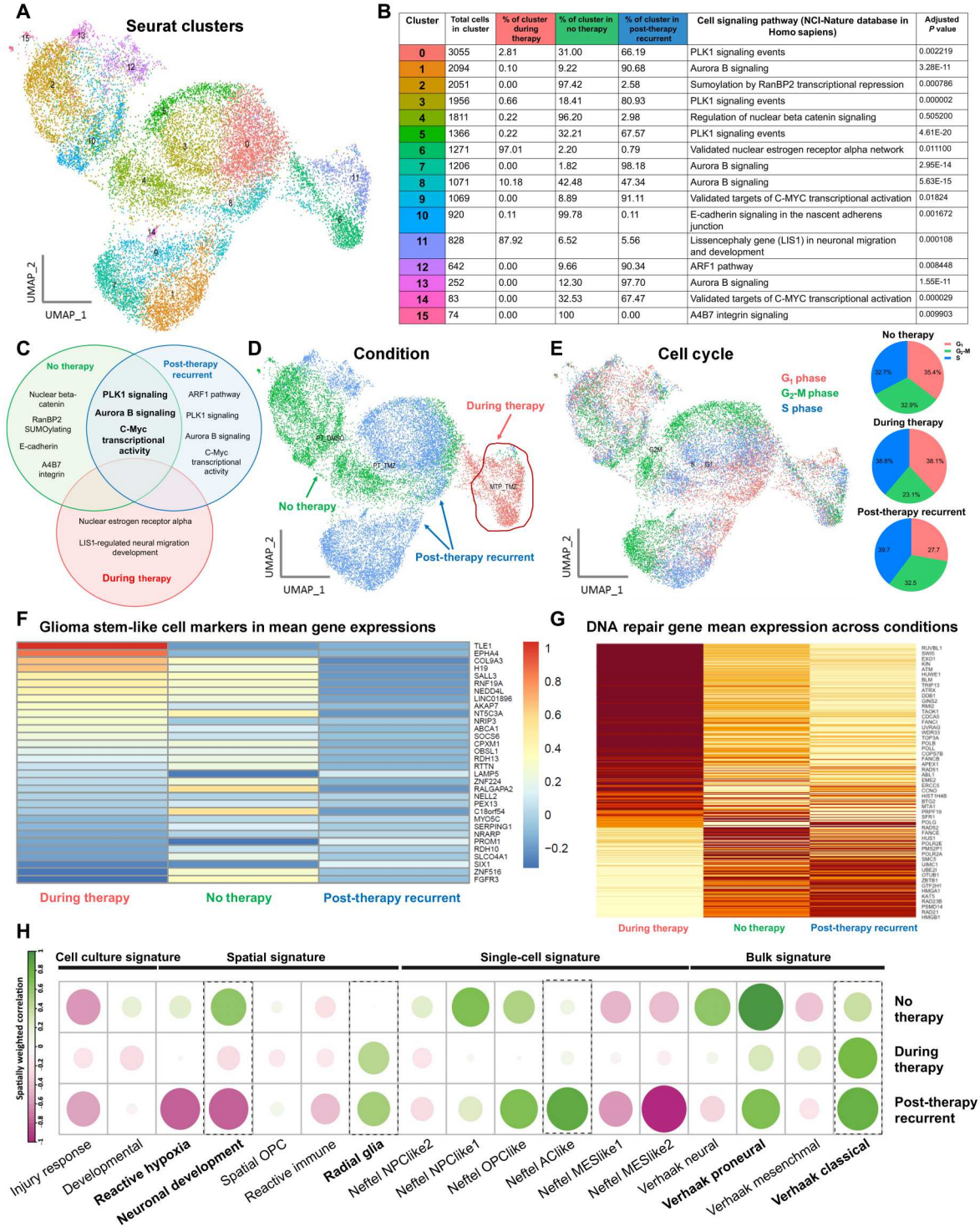

Cluster	Total cells in cluster	% of cluster during therapy	% of cluster in no therapy	% of cluster in post-therapy recurrent	Cell signaling pathway (NCI-Nature database in Homo sapiens)	Adjusted *P* value
0	3055	2.81	31.00	66.19	PLK1 signaling events	0.002219
1	2094	0.10	9.22	90.68	Aurora B signaling	3.28E-11
2	2051	0.00	97.42	2.58	Sumoylation by RanBP2 transcriptional repression	0.000786
3	1956	0.66	18.41	80.93	PLK1 signaling events	0.000002
4	1811	0.22	96.20	2.98	Regulation of nuclear beta catenin signaling	0.505200
5	1366	0.22	32.21	67.57	PLK1 signaling events	4.61E-20
6	1271	97.01	2.20	0.79	Validated nuclear estrogen receptor alpha network	0.011100
7	1206	0.00	1.82	98.18	Aurora B signaling	2.95E-14
8	1071	10.18	42.48	47.34	Aurora B signaling	5.63E-15
9	1069	0.00	8.89	91.11	Validated targets of C-MYC transcriptional activation	0.01824
10	920	0.11	99.78	0.11	E-cadherin signaling in the nascent adherens junction	0.001672
11	828	87.92	6.52	5.56	Lissencephaly gene (LIS1) in neuronal migration and development	0.000108
12	642	0.00	9.66	90.34	ARF1 pathway	0.008448
13	252	0.00	12.30	97.70	Aurora B signaling	1.55E-11
14	83	0.00	32.53	67.47	Validated targets of C-MYC transcriptional activation	0.000029
15	74	0.00	100	0.00	A4B7 integrin signaling	0.009903

Fig. 1. scRNA-seq analysis identifies uniquely expressed genes during TMZ therapy. (**A**) Seurat clusters defined via UMAP dimension reduction of scRNA-seq quality-controlled data were performed in a custom pipeline of Seurat v3.0. (**B**) Table comparing cluster, total cells per cluster, percent of cluster in each treatment condition, NCI-Nature cell signaling pathway of the cluster, and adjusted *P* value. (**C**) Venn diagram created to visualize the indicated unique and overlapping cell signaling pathways enriched in each condition. (**D**) Condition-specific distribution of scRNA-seq data. (**E**) Cell cycling phase of scRNA-seq data. (**F**) Heatmap of the mean expression of up-regulated glioma stem cell markers in our scRNA-seq data. GSEA set: BEIER_GLIOMA_STEM_CELL_UP. (**G**) Representative heatmap of DNA repair–associated genes separated by group condition expressed in our scRNA-seq data. GSEA set: HALLMARK_DNA_REPAIR. (**H**) Spatial correlation analysis between scRNA-seq signatures and gene set signatures. Point size and color indicate spatial correlation.

markers of neuronal development in human GBM tissue, the post-therapy recurrent signature shows a strong anti-correlation, indicating a potential switch between primary and recurrent GBM signatures in their spatial overlap with neurodevelopmental cell signaling pathways. In addition, we see during therapy and post-therapy recurrent signatures to be highly correlated with radial glia markers, which supports recent work investigating the role of outer radial glia-like cancer stem cells contributing to heterogeneity in GBM (*32*).

The spatial correlation of the during therapy transcriptional signature shows an overall weaker spatially weighted signature correlation with established subtypes/states. One possibility is that the transcriptomic profile of during therapy GBM has a unique spatial enrichment and has yet to be characterized in available datasets, supporting the notion that GBM tumors during TMZ therapy remain uncharacterized.

Ribonucleotide reductase gene expression is identified in scRNA-seq analysis

To further investigate molecular mechanisms underlying chemoresistance in GBM, our next goal was to determine targets of interest from our single-cell sequencing data. Our analysis focused on finding transcriptomic differences within conditions to then compare between conditions. Within each condition of our scRNA-seq data, we identified the significant ($P < 0.05$) and uniquely expressed genes that are enriched (logFC > 0.3) or depleted (logFC < −0.3) (fig. S4A). Next, using a combination of gProfiler and Cytoscape, we mapped the pathways associated with genes significantly enriched during therapy (Fig. 2A and fig. S4, A to C). Of several enriched pathways, "Metabolic Processes" ($P < 0.0001$) was one of the top hits for gene expressions enriched in cells from tumors during therapy.

We used STRING to map gene networks involved in metabolic processes found to be elevated during therapy and identified the RNR family of genes (*RRM1*, *RRM2*, and *RRM2B*) that are essential to dNTP metabolism as being significantly enriched (Fig. 2B). The analysis also revealed a strong interaction between the RNR family and inosine-5′-monophosphate dehydrogenase 2 (*IMPDH2*), a key enzyme for purine biosynthesis pathway. As we have previously demonstrated that the IMPDH2-regulated purine pathway contributes to chemoresistance in GBM (*33*), we aimed to investigate the role of RNR-regulated dNTP production in promoting adaption to TMZ during therapy.

Analysis of our scRNA-seq data revealed that while *RRM1* and *RRM2B* remain relatively constant or exhibit a minimal change in no therapy, during therapy, and post-therapy recurrent tumors, *RRM2* increased expression was specific to during therapy tumors (Fig. 2C). We mapped the distribution of cells expressing elevated *RRM2* or *RRM2B* levels in no therapy, during therapy, or post-therapy recurrent GBM, showing *RRM2*-positive cells to be the most elevated during therapy ($P = 0.03$) (fig. S4, D and E). We then examined cells expressing elevated levels of *RRM2* or *RRM2B* with respect to their cell cycle phase and observed that while *RRM2B* remains constant, there are higher levels of *RRM2* in the S ($P = 4.24 \times 10^{-07}$) and G_2-M ($P = 0.0003$) phases (Fig. 2, D and E).

We calculated the percentages of cells expressing elevated levels of *RRM1* and *RRM2* (*RRM1_RRM2*) compared to elevated levels of *RRM1* and *RRM2B* (*RRM1_RRM2B*) to address expression changes in the RNR enzyme subunits throughout TMZ therapy. We observed that cells expressing elevated levels of RRM1_RRM2 are significantly increased in during therapy tumors (91.4%) compared to post-therapy recurrent tumors (58.8%) (fig. S4F). To validate our transcriptional single-cell data of RRM1_RRM2 coexpression through protein level analysis, we used flow cytometry analysis to identify the double-positive population of RRM1_RRM2 in DMSO and TMZ. Results from this experiment align with our transcriptional data and indicate that, on a protein level, RRM1_RRM2 coexpression exhibits a twofold increase in TMZ compared to DMSO ($P = 0.0041$) (fig. S4G).

In examining RNR gene and GSC marker coexpression, we found that cells expressing RRM1_RRM2 have a higher percentage of coexpression with GSC markers across conditions in tumors (Fig. 2F). The trajectories of *RRM1*, *RRM2*, and *RRM2B* gene expression were mapped along pseudotime, with results showing increasing *RRM1* and *RRM2* gene expressions as they progress in during therapy tumors, compared to cells progressing along pseudotime in no therapy and post-therapy recurrent tumors (Fig. 2G). Slingshot analysis of scRNA-seq data revealed the expansion of distinct lineages with respect to treatment time (*23*, *24*). Specifically, sustaining TMZ treatment increased the proportion of cells expressing *RRM2* (fig. S4H).

To examine the basis for RNR subunit expression changes during TMZ therapy, whole-genome chromatin immunoprecipitation (ChIP) was performed in a GBM43 PDX model on day 1 versus day 4 after TMZ therapy tumors. ChIP results show that *RRM2B* expression increases in association with increased histone H3 K4 (H3K4me) monomethylation and histone H3 K27 (H3K27me3) trimethylation. These two markers are up-regulated in combination to both activate and repress transcription, causing the histone to be poised and temporarily stopped (*34*). In contrast, ChIP results showed that *RRM2* expression increases in association with only the H3K4 monomethylation, indicating an activated transcriptional state (Fig. 2H). RNA-seq analysis of bulk tumor RNA revealed that *RRM2* was up-regulated 193× during TMZ treatment ($P = 0.01$), while *RRM2B* was down-regulated 12× during TMZ treatment ($P = 0.03$) (Fig. 2I).

The ribonucleotide reductase gene family affects patient survival and spatial transcriptomic analysis

To better understand RNR gene family expression in clinical samples, we examined publicly available GBM patient datasets. Using GBMseq, a database with GBM single-cell transcriptomic results, we observed cells expressing elevated *RRM2* as being concentrated in the tumor core. In contrast, cells expressing *RRM2B* were identified throughout tumors, i.e., core and periphery (Fig. 3A). We examined mutation profiles of *RRM2* and *RRM2B* using cBioPortal, which revealed that mutation rates were <2% for each gene among 248 patient samples, suggesting that the influence of RNR on GBM tumor biology is not often associated with amino acid sequence changes for these protein subunits (fig. S5A).

Through the GlioVis portal, we analyzed Chinese Glioma Genome Atlas (CGGA) expression data for *RRM2* and *RRM2B*. Using Kaplan-Meier survival analysis, we observed that high *RRM2* expression is inversely associated with patient survival ($P = 0.0012$), whereas *RRM2B* expression level shows no such association (Fig. 3B). In addition, we found that *RRM2* mRNA expression was significantly up-regulated in GBM nontumor brain, whereas

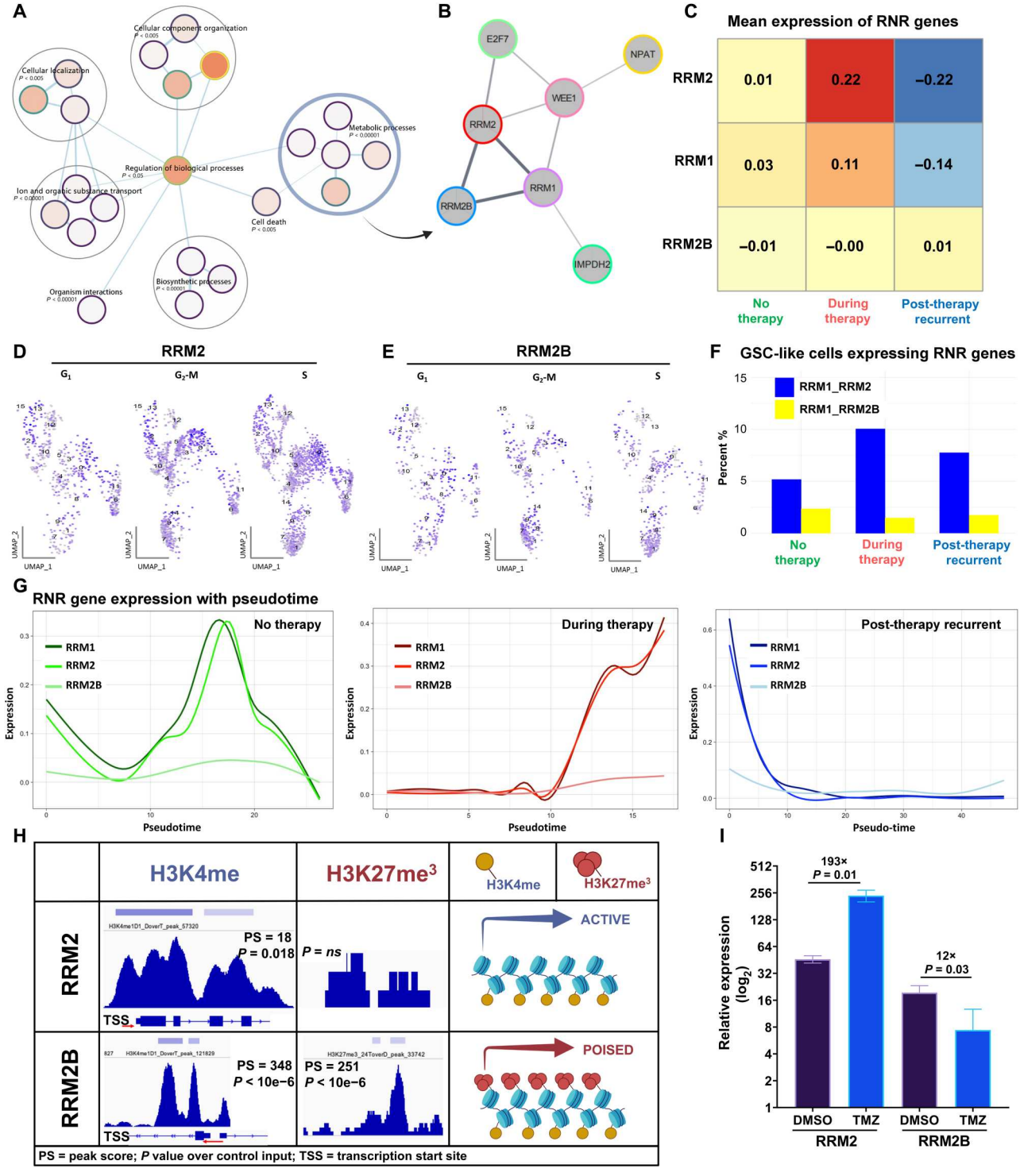

Fig. 2. Ribonucleotide reductase gene expression is identified in scRNA-seq analysis. (**A**) Schematic of pathway analysis significant hits. (**B**) Metabolic genes were found to be among the highest enriched processes during therapy scRNA-seq data, which was further delineated into RNR genes. (**C**) Representative heatmap of the enrichment of specific RNR genes across all three conditions. (**D** and **E**) Complete Seurat cluster data highlighted for cells that were in certain cell cycle phases: G_1 (left), G_2-M (middle), or S (right), and expressed either (D) *RRM2* or (E) *RRM2B*. (**F**) Representative bar graph of the percentage of GSCs in each condition expressing *RRM1_RRM2* or *RRM1_RRM2B*. (**G**) Monocle3 trajectory inference graphs with pseudotime of *RRM1*, *RRM2*, and *RRM2B* gene expressions in no therapy (left), during therapy (middle), and post-therapy recurrent (right). (**H**) Schematic of whole-genome chromatin immunoprecipitation sequencing analysis for H3K4me1 and H3K27me3 at the transcription start site (TSS) of *RRM2* and *RRM2B*. (**I**) mRNA expression of *RRM2* or *RRM2B* in conditions of DMSO or TMZ was analyzed through bulk RNA-seq.

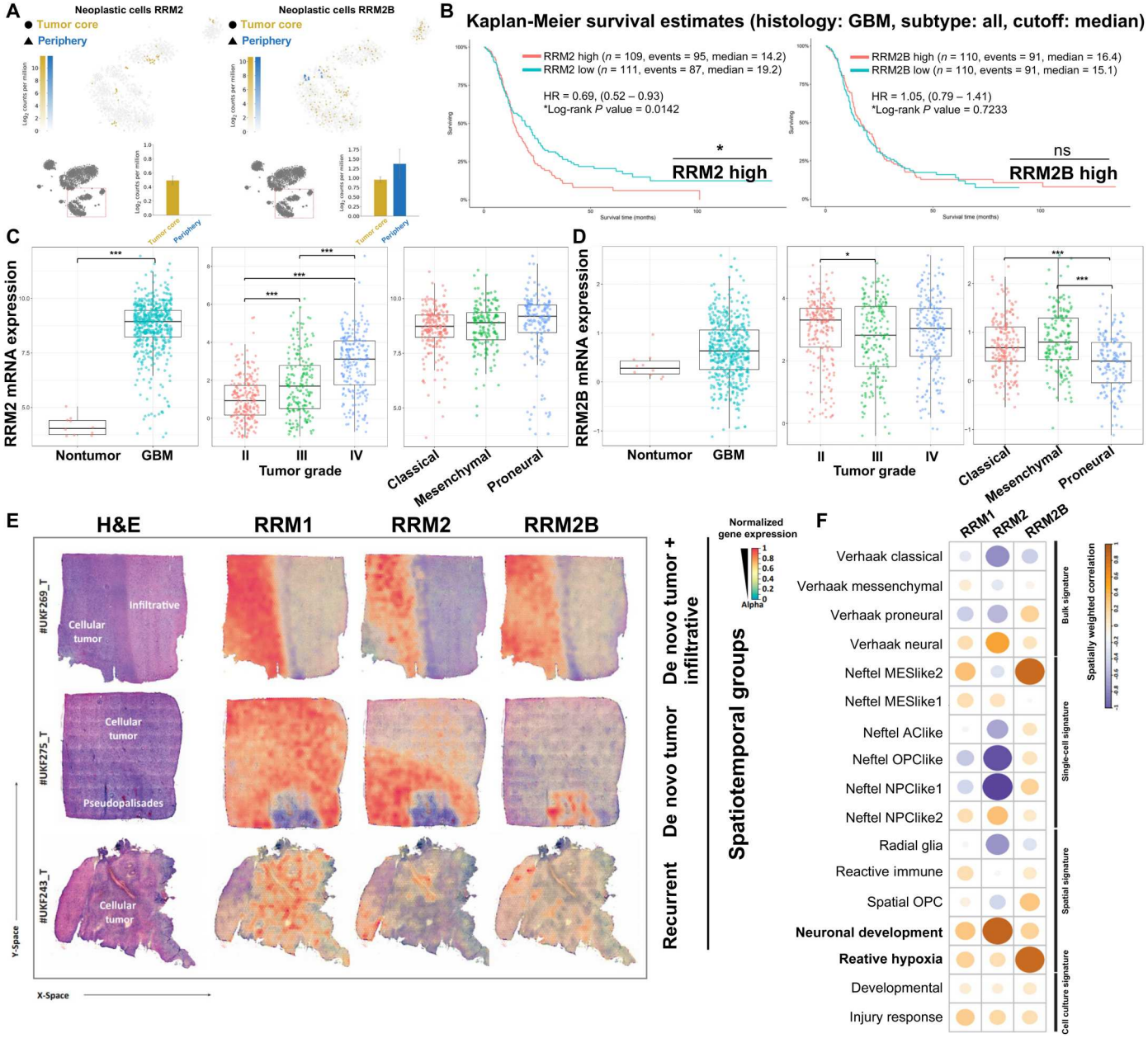

Fig. 3. The ribonucleotide reductase gene family affects patient survival and spatial transcriptomic analysis. (**A**) *RRM2* (left) or *RRM2B* (right) expression in tumor core or periphery. (**B**) Kaplan-Meier survival estimates of high *RRM2* expression (left) versus high *RRM2B* expression (right). (**C** and **D**) GlioVis data was acquired through The Cancer Genome Atlas (TCGA) and Chinese Glioma Genome Atlas (CGGA) databases. (**E**) Surface plots of the *RRM1* (left), *RRM2* (middle), and *RRM2B* (right) expression spatial enrichment. (**F**) Spatial correlation analysis between *RRM1*, *RRM2*, and *RRM2B* and gene set signatures. Point size and color indicate spatial correlation. *$P < 0.05$; ***$P < 0.001$. ns, not significant.

RRM2B mRNA expression is relatively equal for these tissues ($P < 0.001$) (Fig. 3, C and D). *RRM2* expression increased expression with respect to tumor grade (II to IV: $P < 0.001$), while *RRM2B* expression does not show significant change with respect to tumor grade. However, in comparing GBM transcriptional subtypes, we found *RRM2* as well as *RRM2B* expression to be significantly higher among classical and mesenchymal GBM ($P < 0.001$) (fig. S5, B and C). In addition, RRM1 and RRM2 expression show a strong paired correlation in GBM ($P < 0.001$), while RRM1 and RRM2B expression do not ($P < 0.001$) (fig. S5D). Using the Human Protein Atlas, we observed low (<25%) RRM2 and high (>75%) RRM2B cellular staining in post-therapy recurrent GBM tissue (fig. S5E). Immunoblot analysis of GBM PDX and noncancer cell lines showed marked differences in RRM1, RRM2, and RRM2B expression (fig. S5F).

Spatially resolved transcriptomic analysis revealed similarities and differences between where RRM1, RRM2, and RRM2B localize in primary GBM patients' tissue (Fig. 3E). Similarly, RRM1, RRM2,

and RRM2B are all highly enriched in the cellular tumor compartment compared to infiltrative regions. In contrast, when examining the cellular tumor compared to the pseudopalisades, RRM1 is spatially enriched in both regions, RRM2 is spatially enriched in the pseudopalisades, and RRM2B is uniquely localized to the necrotic tumor core. The expression of *RRM2B* in the hypoxic tumor core supports previously published work that identifies the RNR enzyme undergoing a preferential switch in binding to favor RRM2B during hypoxic conditions (*35*).

We then used stRNA-seq to explore the spatial correlation between RNR gene expression and GO gene sets using GSEA, which observed differences in *RRM2* versus *RRM2B* expression (Fig. 3F). For example, when we look at the markers of neuronal development, we see that *RRM2* expression, compared to *RRM1* and *RRM2B*, shows a strong spatial correlation with markers of neuronal development, again indicating possible involvement between developmental signals in oncogenesis (*22*, *36*, *37*).

RNR gene expression is altered during TMZ therapy

After multi-exposure treatments of TMZ or equimolar vehicle control DMSO for 72 hours, GBM PDX cell lines maintained constant RRM1 and RRM2B expression, while RRM2 increased (fig. S6A). These findings are consistent with results from fluorescence-activated cell sorting (FACS) analysis, which shows elevated RRM2 after TMZ ($P < 0.0001$) (Fig. 4A and fig. S6, B and C). RRM1 must bind with either RRM2 or RRM2B for the RNR enzyme to be functional (*17*). We next performed immunoprecipitation using an anti-RRM1 antibody, which revealed increased RRM1-RRM2 binding during TMZ treatment, while RRM1-RRM2B binding showed minimal difference across conditions (Fig. 4B and fig. S6, D and E). To determine the effects of TMZ treatment on RNR subunit stability, we analyzed each subunit level during TMZ treatments that included cycloheximide. This analysis shows RRM2 protein as being more stable than other RNR subunits in cells undergoing TMZ treatment (Fig. 4, C and D, and fig. S6, F and G).

Immunohistochemistry analysis of PDX tissue obtained from vehicle-treated, on treatment, or post-TMZ treatment mice shows RRM2 expression to be significantly higher in GBM during therapy compared to no therapy (GBM39, $P < 0.0001$; GBM43, $P = 0.0012$) or post-therapy recurrent GBM tissue (GBM39, $P = 0.0002$; GBM43, $P = 0.0001$) (Fig. 4E and fig. S6H). In contrast, RRM2B immunoreactivity was similar among the same set of tissues (Fig. 4F and fig. S6I).

RRM2 promotes adaptation to TMZ therapy

To investigate the role of RNR subunits in GBM tumor cells′ response to TMZ, we developed knockdown (KD) cell lines using short hairpin RNA (shRNA) plasmid transfection (fig. S7, A and B). Cell viability assays were performed on each shRNA cell line derivative when treated with increasing doses of TMZ. RRM2-KD cells demonstrated increased TMZ sensitivity ($P < 0.001$) (Fig. 5A and fig. S7C) in association with altered DNA repair capacity compared to the control ($P < 0.001$) (Fig. 5B). In contrast, RRM2B-KD cells demonstrated significant resistance to TMZ ($P < 0.001$) (Fig. 5C and fig. S7D) with consistent DNA repair capacity after TMZ treatment ($P < 0.001$) (Fig. 5D and fig. S7E). When RRM2 was overexpressed, GBM cells became resistant to TMZ therapy with altered DNA repair capacity (Fig. 5, E and F, and fig. S7F). To determine whether the DNA damage response of RRM2-KD sensitivity was specific to TMZ, viability assays were performed using several alkylating agents: CCNU, MNU, and MMS. These drugs, similar to TMZ, create lesions in DNA, which result in genomic instability and trigger repair mechanisms, such as nucleotide recruitment, to repair the damaged DNA (*38*–*40*). The results of these treatments show that RRM2-KD cells do not exhibit the same generalized sensitivity to CCNU, MNU, or MMS, as they do to TMZ. This suggests that the treatment sensitivity of RRM2-KD cells is specific to TMZ compared to other alkylating agents (fig. S8, A and B).

Our laboratory and others have previously shown that therapeutic stress can drive plasticity-induced stemness in GBM (*11*, *41*, *42*). To investigate whether RRM2-KD changes cancer stem cell markers in PDX lines, we used immunoblot analysis for known stemness markers, such as Notch1, cMYC, and SOX2. The results of this analysis show that RRM2-KD decreases the expression of stemness-associated genes (Fig. 5G). RRM2-KD cells were also examined for their neurosphere formation capacity, with results showing that RRM2-KD cells produce significantly fewer neurospheres and decreased neurosphere size across multiple cell lines (Fig. 5H and fig. S9, A to E).

To complement the genetic manipulation experiments, we investigated the pharmacological effects of the second-generation RNR inhibitor 3-AP (Triapine), which is currently U.S. Food and Drug Administration (FDA)–approved and is in clinical trials as an anticancer agent for different human malignancies (*18*). This drug has been demonstrated to cross the blood-brain barrier, thus providing an opportunity for translation (*43*). Immunoblot analysis using a stemness panel and consequent neurosphere assay was performed on cells treated with 3-AP alone and in combination with TMZ. This analysis shows that 3-AP alone or in combination with TMZ decreases stemness protein expression (Fig. 5I and fig. S9F). The neurosphere assay analysis confirmed that cells treated with 3-AP and 3-AP + TMZ could not form spheres in the same capacity as control cells ($P < 0.0001$) and are generally reduced in size (Fig. 5J and fig. S9, G to N).

Cell viability assay results show that 3-AP + TMZ treatment causes significantly more GBM cell death than TMZ alone ($P < 0.0001$) (fig. S9O). Compared to cells treated with TMZ only, 3-AP + TMZ reduces S-phase cells ($P < 0.001$) (fig. S9, P and Q). 3-(4,5-dimethylthiazol-2-yl)-2,5-diphenyltetrazolium bromide (MTT) analysis of GBM6R cells, a cell line made TMZ resistant by multiple cycles of TMZ treatment and treated with TMZ, 3-AP, or a combination, shows not only that 3-AP ($P < 0.0001$) and TMZ + 3-AP ($P < 0.0001$) significantly kill GBM6 cells but also that combined treatment also decreases the survival of TMZ-resistant GBM6R cells (fig. S9R).

In vivo 3-AP (40 mg/kg) in combination with TMZ (2.5 mg/kg) significantly improves survival in intracranially injected GBM43 ($P = 0.0098$), GBM6 ($P = 0.0023$), and GBM39 ($P = 0.0487$) PDX cell lines (Fig. 5K). Furthermore, combination therapy is also effective on a TMZ-resistant recurrent PDX model, GBM6R (Bottom left, $P = 0.0008$), resistant to TMZ therapy (*44*).

RRM2-mediated production of dCTP and dGTP promotes adaptation to TMZ therapy

To elucidate the mechanism of RNR-mediated chemoresistance, we first examined bulk tumor metabolites. Results from this analysis showed that RRM2-KD cells exhibit altered metabolite production, specifically certain dNTPs, compared to controls (fig. S10, A to C).

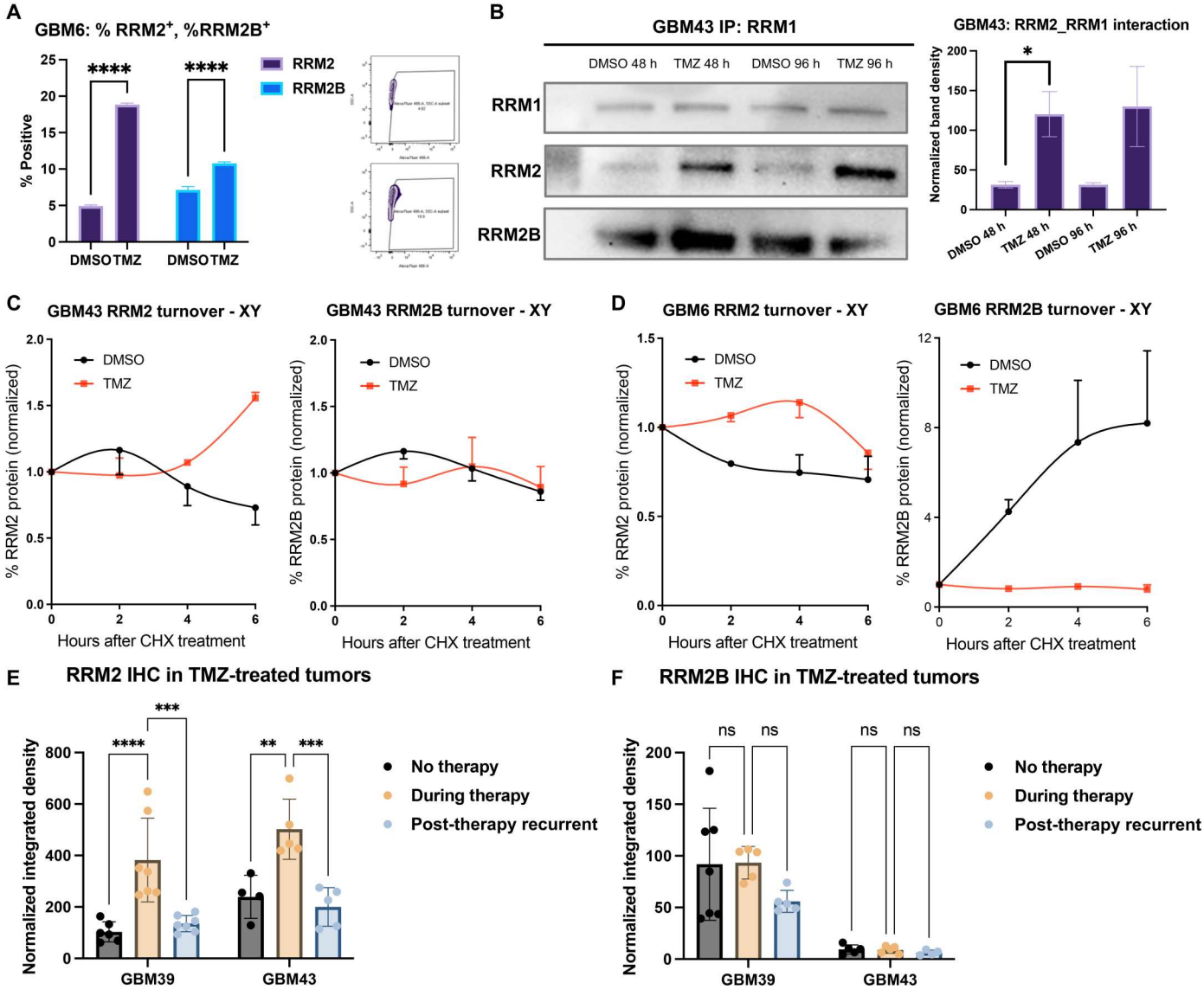

Fig. 4. RNR gene expression is altered during TMZ therapy. (**A**) Representative flow cytometry bar graphs and gates for intracellular RRM2 or RRM2B expression in DMSO or TMZ (50 μM). (**B**) Immunoprecipitation and consequent Western blot analysis of RRM2 and RRM2B binding to RRM1 in DMSO or TMZ (50 μM) for 48 or 96 hours. Using Fiji ImageJ software, RRM2 bands are normalized to RRM1 and bar graph of intraperitoneal interaction was created. (**C** and **D**) Cycloheximide chase assay was performed in GBM43 and GBM6 with DMSO (50 μM) or TMZ (50 μM) for 0, 3, 4, or 6 hours. Representative chase assay graphs of RRM2 (left) and RRM2B (right). (**E** and **F**) Representative bar graphs of immunohistochemistry quantification of no therapy, during therapy, and post-therapy recurrent GBM tissue stained for (E) RRM2 or (F) RRM2B. Images were analyzed using Fiji ImageJ for integrated fluorescent density of the channel (RRM2 as Alexa Fluor 488; RRM2B as Alexa Fluor 647) normalized to the number of cells per image (DAPI). n = 3 independent sets of experiemnts. Validated in GBM39 and GBM43. *P < 0.05; **P < 0.01; ***P < 0.001; ****P < 0.0001.

On the basis of this, we next focused on dNTP signatures, which showed that TMZ treatment increases 2′-deoxyguanosine 5′-triphosphate (dGTP) (P = 0.0004), 2′-deoxycytidine 5′-triphosphate (dCTP) (P = 0.0003), and 2′-deoxyadenosine 5′-triphosphate (dATP) (P = 0.0147) production (3×, 2×, and 2×, respectively) as compared to vehicle-treated control cells. In contrast, RRM2-KD effects were specific in causing significantly less dCTP (P = 0.0005) and dGTP (P = 0.0005) production in response to TMZ (Fig. 6A). In RRM1-KD cells, dNTP production was completely shut down in both DMSO and TMZ, and RRM2B-KD resulted in elevated dGTP in both DMSO and TMZ compared to control (fig. S10D).

Given the alteration in nucleotide synthesis described above, we examined nucleobase transport measured through radioactive flux assays of ^{3}H-guanine and ^{3}H-uridine incorporation into DNA. Results from this analysis reveal that both uridine (P < 0.0001) and guanine (P = 0.0002) are incorporated into RRM2-KD cells to a significantly lesser extent than controls irrespective of treatment, suggesting the idea that, without RRM2, cells are unable to incorporate guanine and uridine into DNA at the same efficiency as control (Fig. 6B and fig. S10E).

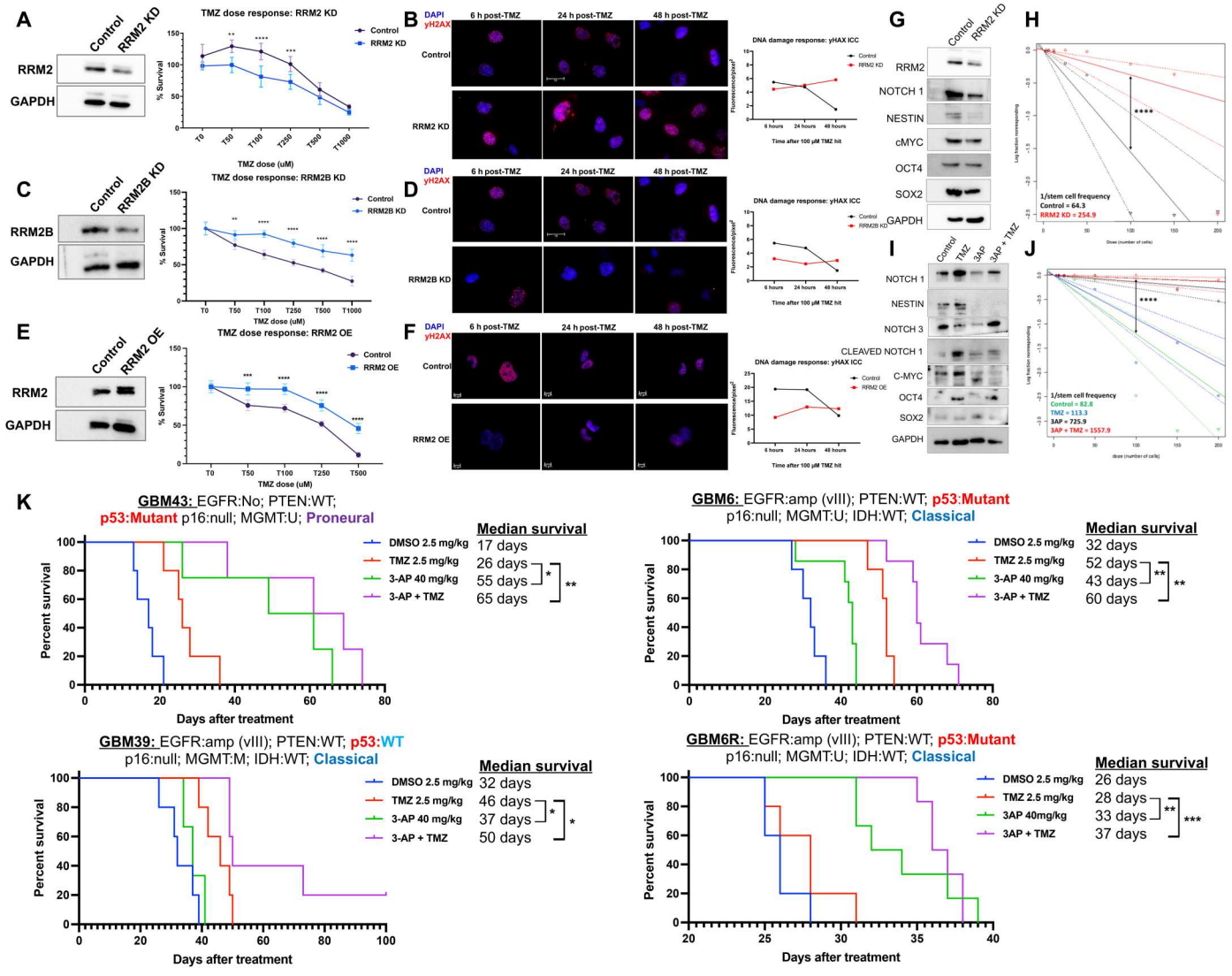

Fig. 5. RRM2 promotes adaptation to TMZ therapy. (**A**) Western blot of RRM2 shRNA KD efficiency. All control cell lines are created by shRNA scramble vectors and are considered shControl. MTT of RRM2-KD in TMZ dose response. (**B**) Immunocytochemistry (ICC) of control versus RRM2-KD cells after 100 μM TMZ treatment. (**C**) Western blot of RRM2B shRNA KD efficiency. MTT of RRM2B-KD in TMZ dose response. (**D**) ICC of control versus RRM2B-KD cells after 100 μM TMZ treatment. (**E**) Western blot of RRM2-OE efficiency. MTT of RRM2-OE in TMZ dose response. (**F**) ICC of control versus RRM2-OE after 100 μM TMZ treatment. (**G**) Western blot of control and RRM2-KD cells. Blots stained for RRM2 and stemness marker genes. (**H**) Extreme limiting dilution analysis (ELDA) plot and table of neurospheres formed in control and RRM2-KD cells. (**I**) Western blot of GBM43 cells treated with DMSO (50 μM), TMZ (50 μM), 3-AP Triapine (2 μM), and TMZ + 3-AP Triapine. Blots stained for stemness marker genes. (**J**) ELDA plot and table of neurospheres formed in GBM43 cells treated with DMSO, TMZ, 3-AP, or TMZ + 3-AP. (**K**) In vivo survival analysis in mice engrafted with GBM cells and treated with DMSO, TMZ, 3-AP, or TMZ + 3-AP. *P < 0.05; **P < 0.01; ***P < 0.001; ****P < 0.0001.

To examine the relationship between RNR subunits and specific dNTP production in a clinical setting, we combined spatially resolved transcriptomic analysis with matrix-assisted laser desorption/ionization (MALDI) mass spectrometry analysis of GBM patients′ tissue. This analysis shows that the localization of cells expressing *RRM1* + *RRM2* is enriched in tumor regions in which cells expressing *RRM1* + *RRM2B* are depleted, confirming in patient samples that the transcription expression pattern of *RRM2* and *RRM2B* is very different (Fig. 6C). Multiomic integration of spatially resolved transcriptomic and metabolomic (MALDI) data shows that cellular coexpression of *RRM1* + *RRM2* correlates with elevated dGTP in patient samples (Fig. 6D). *RRM2* also shows the highest spatial expression correlation with the areas with elevated levels of metabolomic intermediates such as dGTP, adenosine 5′-diphosphate (ADP), uridine 5′-monophosphate (UMP), and *N*-carbamoyl aspartate, indicating the importance of *RRM2* in both purine and pyrimidine biosynthesis (Fig. 6E) (*45*). In contrast, *RRM2B* expression was correlated with dCTP, ADP, and GMP (guanosine 5′-monophosphate). In comparing relationships between metabolic intensity and cell type markers, we find both dGTP and N-carbamoyl aspartate to exhibit the strongest spatial overlap with neural progenitor–like (Neftel_NPClike) cells, suggesting an interplay between migratory mechanisms of NPCs and the metabolic pool promoting GBM tumor growth (*46*).

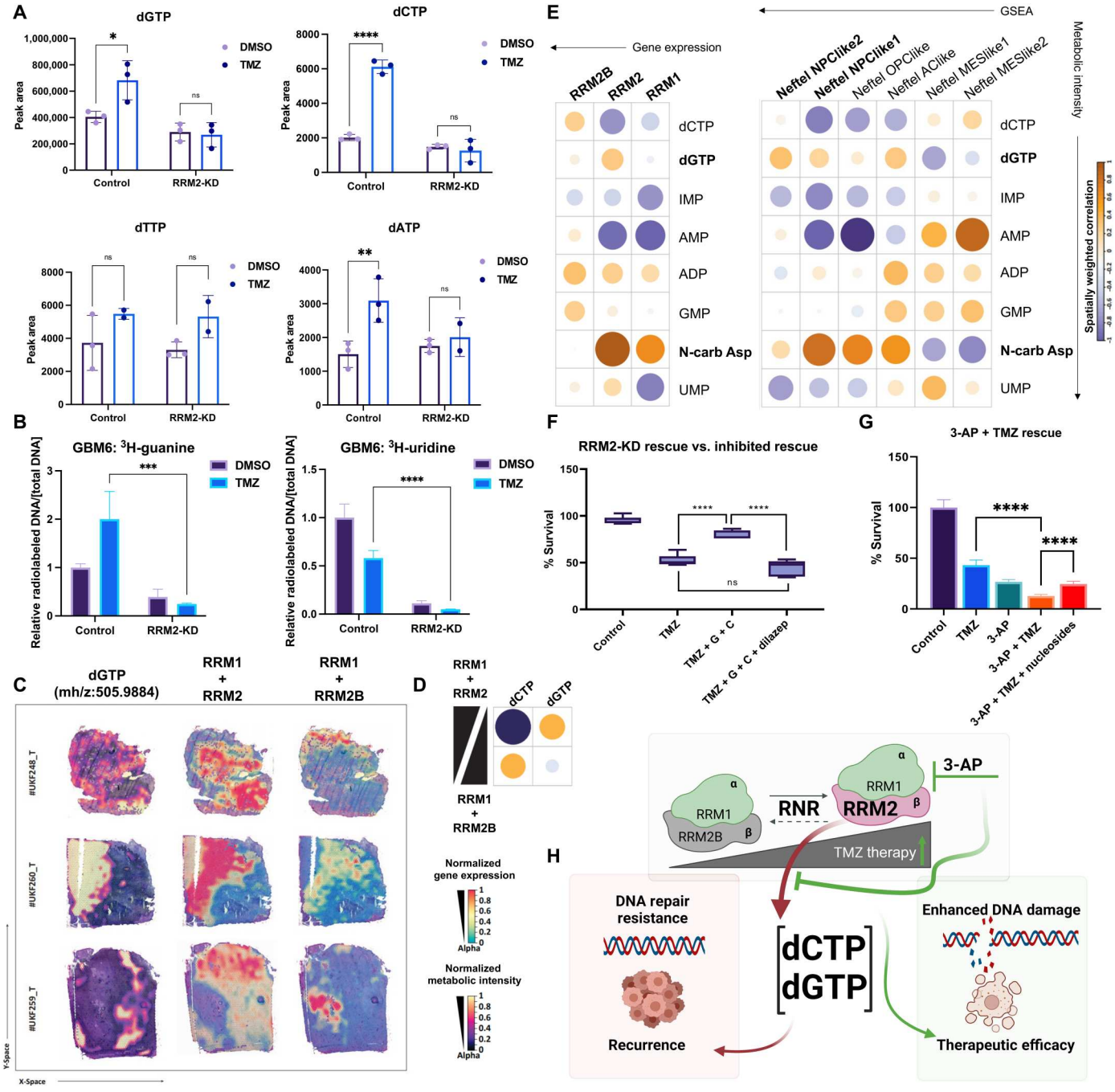

Fig. 6. RRM2-mediated production of dCTP and dGTP promotes adaptation to TMZ therapy. (**A**) Targeted metabolomics of dNTP production in control and RRM2 shRNA KD cells. Control cell lines are created by shRNA scramble vectors and are considered shControl. (**B**) Isotope tracing of ^{3}H-guanine (left) and ^{3}H-uridine (right) in control and RRM2-KD cells. (**C**) Surface plots of the dGTP (left), *RRM1* + *RRM2* (middle) and *RRM1* + *RRM2B* (right) enrichment in GBM patients' tissue. (**D**) Spatial correlation between *RRM1* + *RRM2* or *RRM1* + *RRM2B* expression and dCTP or dGTP enrichment. (**E**) Spatial correlation between *RRM1*, *RRM2*, and *RRM2B* expression and metabolic intensity signatures (left). Spatial correlation between gene set signatures and metabolic intensity signatures (right). Point size and color indicate spatial correlation. (**F**) MTT of RRM2-KD cells when treated with DMSO, TMZ, TMZ + deoxycytidine, and deoxyguanosine nucleosides. Cells treated with TMZ + deoxycytidine and deoxyguanosine nucleosides + dilazep block rescue effect. (**G**) MTT of RRM2-KD cells when treated with DMSO, TMZ, 3-AP, 3-AP + TMZ, or 3-AP + TMZ + deoxycytidine and deoxyguanosine nucleosides. (**H**) Schematic of hypothesis made with BioRender. *P < 0.05; **P < 0.01; ***P < 0.001; ****P < 0.0001.

On the basis of our targeted and bulk metabolomics, we proposed that cellular response to TMZ requires RRM2-mediated specific dNTP production. We next examined whether exogenous nucleoside supplementation during TMZ therapy compensates/rescues GBM cells from the effects of RRM2-KD by protecting them from TMZ-induced toxicity. For this, the medium with RRM2-KD cells was supplemented with deoxycytidine and deoxyguanosine, dephosphorylated forms of dCTP and dGTP, during TMZ treatment. The results revealed that exogenous nucleosides increased cell survival of RRM2-KDs treated with TMZ by an average of 30% ($P < 0.0001$) (Fig. 6F and fig. S10, F and G). To verify that the additional nucleosides were responsible for increased cell survival of RRM2-KDs, we added dilazep, a known nucleoside transport inhibitor, (*47*) to cells treated with TMZ and supplemental deoxycytidine and deoxyguanosine. Dilazep blocking of nucleoside transport nullified the rescue effect of added nucleosides ($P < 0.0001$) (Fig. 6F and fig. S10, F and G). To further establish that nucleoside rescue of RRM2-KD cells was specifically mediated by deoxycytidine and deoxyguanosine, we examined the effects of adding deoxyadenosine and thymine to KD cells, with MTT assay results showing that these nucleosides provided no rescue benefit (fig. S10H).

We found that compared to cells treated with 3-AP and TMZ, cells treated with 3-AP, TMZ, and a supplemental dose of nucleosides could rescue the GBM from TMZ-induced death (Fig. 6G and fig. S10I). We used immunocytochemistry to stain for yH2AX in cells treated with TMZ alone, 3-AP alone, a combination of 3-AP and TMZ, 3-AP + TMZ + additional nucleosides, or vehicle control DMSO. Using ImageJ to quantify yH2AX foci count per cell, per condition, the results show that the addition of deoxycytidine and deoxyguanosine promotes less yH2AX ($P = 0.0097$), indicating less DNA damage and overall cellular death (fig. S10J). Our studies have revealed a previously unidentified approach to targeting the RNR enzyme and identified the corresponding molecular mechanism underlying the success of this approach (Fig. 6H).

DISCUSSION

Selection pressures induced by anticancer therapeutics give rise to the fittest cancer cells that resist chemotherapy and initiate recurrence. Recent studies demonstrated that intratumoral heterogeneity of GBM, driven by transcriptomic plasticity, plays a vital role in cellular adaptations to therapy (*48*, *49*). However, most of the current studies have attempted to investigate the mechanism of adaptation by focusing on two-time points: the treatment naïve primary GBM and the post-therapy recurrent GBM. This is partly due to the lack of access to GBM tissues during chemo- and radiotherapy. However, through an evolutionary lens, the development of therapeutic resistance can be described as a "bottleneck" effect on cancer cell phenotypes, driven by selection pressure during therapy, promoting the emergence of a resistant cell population by increasing the impact of genetic drift (*5*–*8*, *50*). As evolutionary fitness is a continuous process (*51*), it may not be sufficient to elucidate the mechanism of resistance in GBM by focusing on the pre- and post-therapy populations. This study attempts to bridge this gap by examining GBM cellular characteristics during TMZ therapy in a PDX model through single-cell sequencing, spatially resolved transcriptomic analysis, and metabolomic analysis.

Our in vivo scRNA-seq analysis illustrated the unique nature of cells present during therapy compared to no therapy and post-therapy recurrent PDX GBM. Analysis revealed a condition-specific distribution in our data, in which we found that both the active and future transcriptomic profiles of GBM cells during therapy were distinctly clustered from no therapy and post-therapy recurrent transcriptomic profiles. GSEA found that cells during therapy are enriched with GSC markers . Furthermore, of these GSC markers, pathways involved in Notch signaling are highly elevated during therapy . These GSCs contribute to drug resistance and tumor recurrence due to their unique ability to self-renew in dispersed subpopulations and are regulated by many of the same neurodevelopmental mechanisms that regulate stem cell development, i.e., the Notch signaling pathway (*20*, *52*, *53*). Our data provide evidence of drug-induced stress-modulating stemness properties and plasticity, specifically during TMZ therapy in GBM at the single-cell level.

We next identified functional differences across scRNA-seq states, in which we see distinct clusters of DNA repair and resistance gene sets highly expressed during therapy while expressed at low levels in no therapy and post-therapy recurrent GBM. In general, DNA repair and therapy resistance have been investigated at large in cancers, including GBM, in which DNA repair mechanisms are critical in removing toxic lesions produced through chemo- and radiotherapy (*54*). In support of previous data addressed by this laboratory (*33*), our data underline the dynamic shift in expression of these DNA repair and resistance genes throughout TMZ therapy in GBM.

We then used an in silico multidimensional approach integrating our scRNA-seq signatures for each time point with spatially resolved transcriptomic analysis in 16 patient samples. Our analysis identified distinct spatial compartmentalization of GBM signatures for no therapy, during therapy, and post-therapy recurrent. Before and during TMZ therapy, cell signatures are diffusely correlated across all tumor regions; however, by the time cells are in their post-therapy recurrent state, they shift into a strong spatial correlation with cell signatures located in pseudopalisading tumor areas. As previous literature has shown, GBM subtypes are molecularly distinct, and the progression into each subtype may be influenced by therapy (*54*–*57*). Our analysis shows cells characterized without therapy to be highly correlated with the proneural subtype, which was the original molecular classification of our PDX model (*25*). Cells during therapy show molecular signatures drifting toward the classical subtype. However, cells in the post-therapy recurrent state displayed both proneural and classical signatures. These results indicated that the molecular subtype is dynamic and can change with TMZ therapy.

During therapy, we have also identified the unique signature of the RNR family of genes; while *RRM1* and *RRM2B* remained relatively constant across conditions, *RRM2* expression was significantly elevated during therapy. This is an interesting finding, as the role of RRM2B in p53-mediated DNA damage response has been extensively reported in the literature (*58*–*60*). However, a recent pan-cancer metabolic analysis found *RRM2* as one of the highest gene expressions across 16 tumor types and shows eightfold higher expression in cancer tissue compared to matched normal tissue (*61*). Although the RNR enzyme itself, essential for dNTP metabolism, has been extensively studied, the role of specific RNR subunits in mounting response to chemotherapy is not well understood. From our initial analysis, we proposed that the enzyme

undergoes a preferential switch in subunit binding to favor RRM2 during TMZ therapy.

In vitro, we found that RRM2-KD cells promote a TMZ-sensitive phenotype in GBM cells, while RRM2B-KD cells caused TMZ resistance. In contrast, RRM2-overexpression (RRM2-OE) cells reversed the TMZ sensitivity of KD cells, producing a TMZ-resistant phenotype. Moreover, RRM2 expression is associated with stemness, as RRM2-KD was associated with reduced expression of stemness genes as well as decreased neurosphere formation capacity of GBM cells. The correlation between RRM2 and regulated cellular plasticity remains elusive in research. It is not clear if the RRM2-regulated cellular plasticity is a cause or a consequence. We postulate that such correlation lies in the ability of RRM2 to regulate the demand for dNTPs during TMZ therapy and elevated overall stemness in GBM populations during TMZ therapy. Previous publications hypothesize that GSCs quickly respond to therapeutics and adapt to enforce resistance, supporting tumor growth and recurrence (*62*–*64*). Perhaps, RRM2 regulates both the metabolic availability for GSC-like cells and allows them to respond to TMZ therapy, contributing to chemoresistance and GBM recurrence.

Metabolic flux dynamics have been briefly explored in TMZ-resistant GBM (*65*), but how TMZ alters the dNTP metabolism in GBM is an understudied topic. Our study found that GBM cells markedly increased dGTP and dCTP levels in response to TMZ treatment, while RRM2-KD cells failed to produce dGTP and dCTP and became sensitive to TMZ therapy. We can rescue this TMZ sensitivity by exogenously adding deoxyguanosine (dGDP) and deoxycytidine (dCDP), the nucleoside counterparts of dGTP and dCTP, respectively. In addition, 3-AP, an FDA-approved RRM2 inhibitor, sensitizes GBM cells in vitro and in vivo, leading to significant survival in GBM tumor–bearing mice treated with a combination of 3-AP + TMZ.

The contribution of RNR-mediated dNTP synthesis is critical for mounting effective cellular DNA damage response, which relies on the p53-dependent expression of the RRM2B subunit (*59*, *66*). However, as p53 is one of the most frequently mutated genes in all cancer, including in 30% of GBMs (*67*), it is conceivable that cells may use an alternative pathway for dNTP production in response to DNA damage. Our preliminary data demonstrated that during TMZ therapy, GBM cells transiently switch from RRM2B to RRM2 via epigenetic mechanisms to generate specific dNTPs (dCTP and dGTP) to alter the DNA repair capacity and possibly mount chemoresistance. This is a previously unknown mechanism of selectivity for dNTP synthesis in response to TMZ-induced DNA damage.

Previous literature has identified BRCA1-mediated expression of RRM2 to play a protective role in GBM cells against endogenous replication stress and DNA damage (*68*). However, in our single-cell analysis, we do not find *BRCA1* to be enriched during TMZ therapy, thus concluding that RRM2 expression during TMZ therapy may be independent of BRCA1 expression.

To reveal the clinical significance of our proposed mechanism, we examined whether a molecular switch in RNR subunit binding physically manifested as histological consequences in silico. Specifically, we analyzed the spatial distribution of RNR gene expression across distinct GBM patients′ tumor regions. We observed that *RRM2* localizes to the hypoxia core-periphery, while RRM2B strongly localizes to the hypoxic tumor core. This phenomenon is supported by Foskolou *et al.* (*35*), in which authors demonstrated a switch from RRM2 to RRM2B under hypoxic conditions.

Moreover, we observe a positive correlation between *RRM2* and GBM cells with neuronal development signatures. Unregulated cell signaling pathways associated with neurodevelopmental signatures have been shown to be involved in gliomagenesis (*37*, *56*, *69*, *70*). Still, the role of *RRM2* in GBM cells with neuronal development signatures has yet to be reported. Our analysis indicates that *RRM2* is associated with metabolic adaptation to chemotherapy and GBM cells with neuronal development markers, suggesting that mechanisms of neurodevelopment and oncogenesis might work in parallel to support brain tumor resistance and progression.

It remains unclear why there is a need for specific dNTPs during TMZ therapy or the mechanism of RRM2 selectivity toward producing specific dNTPs. Previous studies have shown that distinct DNA repair pathways are required for specific types of DNA damage and that each DNA repair pathway has a unique mechanism of action and substrate specificity (*71*). For example, O^6-methylguanine (O^6-MG) is the critical site of nucleotide damage caused by TMZ therapy, and GBM cells can sense depletion in their purine nucleotide pools (*33*). It is possible that RRM2-mediated de novo synthesis of dGTP is required when GBM cells are depleted of nucleotides because of TMZ-induced O^6-MG damage. However, this specificity needs to be investigated further.

Although the mechanism underlying dNTP selectivity requires further study, our data, first shown in vitro and now with clinical evidence, indicate that RRM2 promotes dGTP production. Using multidimensional stRNA-seq data, we observed strong colocalization of *RRM2* and dGTP in clinical GBM samples, indicating the importance of RRM2 in maintaining specific metabolic pools in GBM tumors as we can visualize the spatial specificity of *RRM2* localization to regions of high dGTP intensity. We also see a strong spatial correlation between dGTP intensity and neural progenitor–like cells (NPCs), indicating a relationship between NPC-like GBM cell proliferation or migration and dGTP pools, suggesting the possibility of NPC-driven resistance as a dGTP-associated mechanism (*72*, *73*). Our in silico analysis thus confirms the importance of RRM2-mediated tumor metabolism in GBM and provides insight into the metabolic dynamics between neural and tumor development in the brain.

In conclusion, through the characterization of GBM during TMZ therapy, we present a mechanism of metabolic adaptation in GBM that drives chemoresistance and the corresponding druggable target that can be inhibited to enhance the efficacy of TMZ therapy in the clinic. We provide previously unknown evidence regarding RRM2-regulated dGTP adaptations during TMZ therapy, contributing to the growing understanding of the cross-talk between metabolism, cellular response to drugs, and chemoresistance in GBM. As demonstrated in our study, exploiting the metabolic vulnerabilities of GBM tumors and informing such exploit through multidimensional analysis of clinical samples lead to an advanced understanding of a chemoresistant mechanism in GBM and an auspicious clinical opportunity to improve the outcomes for patients harboring this deadly disease.

MATERIALS AND METHODS

In vivo scRNA-seq model

Athymic nude mice were acquired from Charles River Laboratories (nu/nu; Charles River, Skokie, IL, USA) and housed according to Institutional Animal Care and Use Committee (IACUC) standards defined by Northwestern University (*74*). Before intracranial implantation of GBM43 PDX line, all mice were confirmed anesthetized via administration of ketamine and xylazine. Tumors were placed 3 mm into the cortex of the mouse through a burr hole, and the incision was closed using sterile sutures. Upon recovery from anesthetic, analgesics were administered, and mice were observed to be bright, alert, and reactive. In total, 150,000 GBM43 cells were injected per mouse, and an incubation period of 7 days was given for PDX cells to establish a tumor before any therapy began.

After the 7-day incubation period, mouse groups were divided equally based on sex to receive TMZ or DMSO (2.5 mg/kg) (vehicle control) given intraperitoneally for 5 days total. During day 3 of TMZ treatment, a group of mice was sacrificed, and their tumors were biopsied and taken for single-cell processing, which represents the during therapy time point within the study. Last, after the 5-day dosing period was complete, the mice were monitored until symptoms of the tumor became evident, at which point they were sacrificed, and the tumors were processed for single-cell analysis. The mice that received DMSO for 5 days and were sacrificed at their endpoint represent the no therapy time point, and the mice that received TMZ for 5 days and were sacrificed at their endpoint represent post-therapy recurrent time point in the study.

Single-cell processing and drop sequencing

After the mice were sacrificed due to tumor burden, the tumor bulk and margins were dissected using a surgical technique. Tumors were then enriched for human cells using a Miltenyi Mag bead purification kit specific to human leukocyte antigen (HLA) to separate mouse cells that could have invaded the PDX tumors. This process was done according to the manufacturer's instructions as supplied with the kit. After HLA purification, a count of live cells was obtained, and cells were prepared to be run through the DropSeq microfluidic device.

For DropSeq, we followed the protocol set forth by Macosko *et al.* (*75*). Briefly, cells were captured during a 15-min droplet run on a clean microfluidic chip in an unused lane. Droplets were imaged for quality and to ensure that minimal doublets were present. Droplets were then broken, and library preparation was conducted for single-cell sequencing.

Bioinformatic analysis

The bulk of single-cell data bioinformatic analysis was done in Seurat v3.0 (*76*). A custom pipeline was used to score cells on their ability to align to mouse and human genomes to bioinformatically determine whether our magnetic bead purification could not eliminate mouse cell invasion in samples. For preprocessing, FASTQ files from the DropSeq experiments were run through DropRunner, a universally available pipeline for processing scRNA-seq data from either DropSeq or 10x platforms (*77*).

To fully filter out any mouse cell contamination that may have made it through our purification steps, the FASTQ files were separately aligned to both human and mouse genomes producing a species score ranging from 0 to 100 (closer to 0 indicating strong alignment with mouse and more comparable to 100 indicating strong alignment with human). This score was captured for each cell, stored in the Seurat object metadata, and used as an initial data subset to capture only cells with a score greater than 80. Further filtering of the initial cell set was done on the basis of the calculation of a mitochondrial read score and on the total number of features captured per cell (mitochondrial read score < 0.20, number of features captured > 250) as is done in the standard Seurat workflow (*78*). After filtering, all samples were merged into one Seurat object using the Merge function, and normalization was done on the object via the NormalizeData function. We searched for the top 2000 variable features using the FindVariableFeatures process and then scaled the data regressing on features captured and mitochondrial read score to prepare for PCA. All 2000 variable features captured were used as input for PCA. The top 20 PCs were computed, and both elbow plots and JackStraw tests were completed to assess their validity.

We used the FindClusters function across all 20 PC dimensions with a resolution of 0.6 to determine clustering for Uniform Manifold Approximation and Projection (UMAP). At the same time, t-distributed stochastic neighbor embeeding (t-SNE) clusters were selected with all 20 measurements and perplexity set to 30. Last, for dimensional reduction plotting, both t-SNE and UMAP were used.

Pseudotime analysis

Analyzed scRNA-seq data were clustered using the custom Seurat pipeline, and trajectories between these clusters were determined using Monocole3. Using the program to determine the appropriate starting point, pseudotime was calculated as a distance along trajectories from the starting point, measuring genetic variance for each cell compared to the starting point gene signature. Pseudotime graphs were then generated as a plot of condition-normalized raw counts per cell of the gene or pathway of interest for each cell as a function of pseudotime for each cell.

Enrichment mapping

Enrichment mapping was performed using gProfiler and Cytoscape. Genes of interest were first inputted into gProfiler, and the appropriate enrichment functional pathways were selected. The outputted GEM file was then uploaded into Cytoscape using the EnrichmentMap extension, which generated a base EnrichmentMap with enriched pathways and their corresponding significance (*P* value). Last, pathways were grouped and represented as a figure.

Cell lines and culture

A human glioma cell line, U251, was procured from the American Type Culture Collection (ATCC; Manassas, VA, USA). To culture the cells, Dulbecco's modified Eagle's medium (DMEM; Corning, Corning, NY, USA)—containing 10% fetal bovine serum (FBS; Atlanta Biologicals, Lawrenceville, GA, USA) and 1% penicillin-streptomycin antibiotic mixture (Cellgro, Herndon, VA, USA; Mediatech, Herndon, VA, USA)—was used (*74*).

PDX glioma cell lines (GBM6, GBM6R, GBM39, and GBM43) were obtained from C. D. James at Northwestern University. Cells were maintained according to the protocol (*74*). However, the PDX cells were cultured in DMEM composed of 1% FBS and 1% penicillin-streptomycin. A frozen stock, maintained in liquid nitrogen at

−180°C in pure FBS supplemented with 10% DMSO, was used to replenish cells that had reached a maximum of four passages.

Animals and in vivo models

Athymic nude mice (nu/nu; Charles River, Skokie, IL, USA) were used in this study and housed in compliance with IACUC requirements along with federal and state statutes (*74*). Animals were housed in cages equipped with food and water and subjected to a 12-hour light and dark cycle.

Intracranial implantation of GBM cells was conducted according to our laboratory′s previously established GBM mouse model (*74*). The animals first received Buprenex and Metacam by intraperitoneal injection. They were then anesthetized from the second injection of ketamine/xylazine mixture (Henry Schein, New York, NY, USA). To confirm that sedation was complete, a toe-pinch was conducted. Next, Betadine and ethanol were applied to the scalp for sterilization, and artificial tears were applied to each eye. The skull was then exposed by creating a small incision using a scalpel, where a ~1-mm burr hole was drilled right above the right frontal lobe. The mice were then placed in a stereotactic rig, where, for 1 min, 150,000 GBM43, GBM6, or GBM39 cells, loaded in a Hamilton syringe, were injected 3 mm from the dura. The needle was raised slightly and left for an additional minute to ensure that the cell suspension was released. The syringe was removed slowly, and the scalp was closed with sutures (Ethicon; Cincinnati, OH, USA), maintaining a consistent position of the head throughout the closing process. Animals were placed on heating pads until awake and responsive.

Drug treatments were initiated 1 week following the implantation in the following manner: intraperitoneal injections of either TMZ (2.5 mg/kg) or equimolar DMSO each day for five consecutive days. Experimental groups were formatted as follows: TMZ (five mice), DMSO (five mice), 3-AP (40 mg/kg) (five mice), TMZ (2.5 mg/kg) and 3-AP (40 mg/kg every other day for 5 days) (four to seven mice), and TMZ (2.5 mg/kg) and 3-AP (40 mg/kg every other day for five treatments) (four to seven mice). Triapine injections were always administered 6 hours before TMZ in the treated mice. Throughout the treatment period, signs of tumor progression were observed and recorded, including weight reduction, hunching, and reduced body temperature. According to IACUC and Northwestern University guidelines, animals were sacrificed once it was evident that they would not survive past the next morning (*74*).

Immunofluorescence

Following euthanasia, mice were supplied with ice-cold phosphate-buffered saline (PBS). After, their brains were frozen in cryoprotectant on dry ice, kept at −80°C, sectioned at 8 μm per section, and stained according to immunohistochemistry protocol (*74*). Sections were thawed at room temperature for 15 to 20 min and then washed two times for 5 min, each in PBS + 0.05% Tween 20 (PBS-T) to eradicate any cryoprotectant. Each brain section was encircled with an immune pen. After that, sections were fixed in ~100 μl of 4% paraformaldehyde (PFA; Thermo Fisher Scientific, Rockford, IL, USA) at room temperature for 15 min and then washed two times for 5 min each. For 1 hour at 37°C, these sections were put in 2 N HCl, and then to neutralize the HCl, they were put in a sodium borate buffer for 30 min. Using PBS-T, the sections were washed three times for 5 min and then, for 1.5 to 2 hours at room temperature, blocked and permeabilized in a 10% bovine serum albumin (BSA) solution with Triton X-100 (Thermo Fisher Scientific, Rockford, IL, USA). Subsequently, the sections were washed three times for 5 min and incubated overnight at 4°C with ~100 μl of primary antibodies diluted in 1% BSA + Triton X-100 (Thermo Fisher Scientific, Rockford, IL, USA). The following morning, the sections were washed three times for 8 min each in PBS. After adding ~100 μl of secondary antibodies diluted in 1% BSA + Triton X-100 (Thermo Fisher Scientific, Rockford, IL, USA), the sections were incubated for 2.5 hours at room temperature. They were washed in PBS-T three times for 10 min each. To image the slides using a Leica microscope, a drop of ProLong Gold Antifade reagent with 4′,6-diamidino-2-phenylindole (DAPI) was added to each section (Thermo Fisher Scientific, Rockford, IL, USA). Images of these slides were compiled and analyzed in ImageJ.

Using the immunocytochemistry protocol (*79*), additional experiments were conducted. After removing plates from incubation and washing once with PBS, 200 μl of 4% PFA was added to each section for 10 min. Next, cells were washed gently with PBS and then blocked for 2 hours at room temperature in 200 μl of 10% BSA solution. Subsequently, the BSA was aspirated off the slides, and 100 μl of primary antibody (mixed with 1% BSA) was added. Overnight, the cells were incubated at 4°C. The following morning, the cells were washed three times for 5 min each in 1% BSA, after which 200 μl of secondary antibody was added to each section. Then, for 2 to 3 hours, the plate was incubated at room temperature. After the incubation, cells were washed three times for 5 min each in PBS. Last, a drop of ProLong Gold Antifade reagent with DAPI was added to each section, allowing the slides to be imaged using a Leica microscope. These images were compiled and analyzed in ImageJ.

Cell viability assays

Viability assays were conducted using a previously established protocol (*80*). Cells were briefly plated at 3000 per well in a 96-well plate with six to eight replicates per condition. Cells were allowed 24 hours for attachment, after which they were treated with varying doses of TMZ from 0, 50, 100, 250, 500, to 1000 μM of TMZ using our laboratory′s standard dose-response protocol (*74*). Following 48 hours of treatment, the medium was removed, and MTT solution was added to the cells. This MTT solution was made by diluting the MTT stock reagent at 5 mg/ml in Dulbecco′s PBS. Next, this MTT stock was diluted in fresh medium at a stock: medium ratio of 1:10. From the formulated mixture, 110 μl was added to each well, and cells were incubated at 37°C for 3 to 5 hours. The medium and MTT stock solution were carefully removed after incubation without pipetting down or aspirating to avoid the possible disturbance of any formed crystals. Next, cells were resuspended in 100 μl of DMSO until the wells turned purple, indicating that the crystals had dissolved. The plate was left at room temperature for 10 min. It was then read on the plate reader at an absorbance of 570 nm; data were analyzed to find percent viability in each well.

Cellular transfection

To generate lentiviral particles, low-passage X293 cells (ATCC, Manassas, VA, USA) were plated at 70% confluency based on a previously cited protocol (*74*). After 6 hours, these cells were then transfected using a mix of HP DNA Transfection Reagent (Sigma-Aldrich, St. Louis, MO, USA) diluted in Opti-MEM medium (Gibco, Waltham, MA, USA) as well as second-generation packaging and shRNA plasmids (Dharamazon), according to the

manufacturer's instructions. After maintaining the transfected X293 cells in culture for 48 to 72 hours, the virus supernatant was harvested. Next, this supernatant was sterilized with a 45-μm filter and ultracentrifuged at 133,897 relative centrifugal force (RCF) for 2 hours. Last, the resulting viral pellet was resuspended in PBS and aliquoted for future use.

Viral transduction

Using a previously optimized protocol, we resuspended cells in a small volume (~50 μl) of medium and added ~10 to 20 multiplicity of infection (MOI) lentivirus amounts per sample (*81*, *82*). Next, this virus-medium mixture was spun for 2 hours at 37°C at 850 RCF, after which these cells were plated and maintained in culture with regular medium changes for 48 to 72 hours. To assess the efficiency of the resulting conditions, Western blots were used.

Western blotting

Per the protocol, cells were treated, detached using trypsin, washed with PBS, and resuspended in mammalian protein extraction reagent (M-PER; Thermo Fisher Scientific, Rockford, IL, USA) (*83*). M-PER was supplemented with protease and phosphatase inhibitors (Thermo Fisher Scientific, Rockford, IL, USA). After aggressively vortexing these cells for 3× 1-min increments, with 10 min of rest on ice between each vortexing, the resulting lysates were spun at 13,000 rpm for 10 min at 4°C. The supernatant was then collected, and the protein concentration for each Western blot was specified via bicinchoninic acid assay (Thermo Fisher Scientific, Rockford, IL, USA). Each sample was composed of equal amounts of protein and varying amounts of SDS buffer (SDS sample buffer; Alfa Aesar, Ward Hill, MA, USA) supplemented with β-mercaptoethanol and water, which allowed for each sample to contain the same total volume. After mixing each sample, they were boiled at 95°C for 10 min.

After running through 8% SDS–polyacrylamide gel electrophoresis (SDS-PAGE; made in-house) by gel electrophoresis (Bio-Rad, Hercules, CA, USA), the proteins were transferred, using a transfer machine, onto 0.45-μm polyvinylidene difluoride membranes (Millipore, Darmstadt, Germany). Following the transfer, these membranes were washed three times for 10 min each in PBS and then blocked with tris-buffered saline (TBS) consisting of 5% powdered milk and 0.05% Tween 20 (Sigma-Aldrich, St. Louis, MO, USA). This blocking lasted 2 hours, after which the membranes were cut according to the proteins of interest. Next, the membranes were placed into primary antibody solutions containing the appropriate antibody to 5% BSA solution supplemented with sodium azide and incubated overnight on a shaker at 4°C. The following morning, these membranes were washed and incubated for 2 hours in a secondary antibody diluted 1:4000 in 5% milk. Subsequently, the membranes were washed three times for 10 min each and coated with enhanced chemiluminescence (ECL; Clarity ECL, Bio-Rad). Using x-ray film, images were developed.

Immunoprecipitation

A mixture of 3 to 5 μl of rabbit immunoglobulin G antibodies and 100 μg of protein sample against ubiquitin, brought to a final volume of 250 μl with M-PER buffer, was incubated to produce beads according to the immunoprecipitation protocol we followed (*84*). Samples were stored in Eppendorf tubes and placed in a rotary shaker in a cold room overnight. The following day, 30-μl beads were administered to the intraperitoneal reaction. Samples continued to be rotated for 2 hours at room temperature. Tubes were centrifuged for 1 min at 1000 rpm, and the supernatant was discarded. Next, beads were washed three times with 1 ml of 0.2% TBST (TBS–Tween 20) wash buffer and centrifuged at 1000 rpm for 1 min. This procedure was carried out three times, with the supernatant discarded preceding each repetition. After the third and final wash, elution buffer was warmed in a 47°C water bath, and 50 μl of elution buffer was added to samples, resuspended, and incubated at 55°C for 10 min to elute protein from beads. After being incubated at 55°C for 10 min, recovered proteins were centrifuged at 3200 RCF for 5 min to dissociate the beads from the supernatant. The supernatant was collected, and the above elution process was repeated. Tubes were centrifuged again at 3200 RCF for 5 min. Last, the supernatant was added to the newly labeled tube to reach a volume of 100 μl of supernatant. Next, 10 μl of 1 M NaOH neutralization buffer was added to each sample. Then, 28 μl of 4× SDS was added to each sample. The samples were then boiled at 95°C for 10 min. Western blots were then run for the analysis of precipitated proteins.

Flow cytometry

Cells were collected in a 96-well V-bottom plate and spun down to a pellet. Cells were then washed with 100 μl of PBS. Primary antibodies (in FACS buffer, 50 μl per well) were added at room temperature in darkness for 1 hour. Cells were spun into a pellet and washed again with 100 μl of PBS. The cells were resuspended in 80 μl of FACS analysis buffer. Cells were spun down again, fix perm buffer was prepared (one-part fix/perm, three-parts buffer), and 100 μl of fix perm was added to each well. Samples were incubated for 20 min at room temperature in darkness. Next, 1:10 diluted perm buffer was prepared in double-distilled water, and 100 μl of perm buffer was added on top of fix/perm. Samples were incubated for 10 min in darkness at room temperature. Samples were spun down for 5 min at 1500 rpm and washed with 1:10 perm buffer. Primary antibody was added in perm buffer (50 μl per well) and incubated overnight at 4°C. Samples were then washed three times with FACS buffer. A secondary antibody was added to the FACS buffer for 1 hour at room temperature in darkness. Samples were washed and resuspended in 100 μl of FACS buffer. Samples were then analyzed on the BD LSRFortessa Cell Analyzer.

Metabolomic isolation and liquid chromatography–mass spectrometry profiling

Extracts were prepared and analyzed by liquid chromatography–tandem mass spectrometry (LC-MS/MS) to measure the relative abundances of specific intracellular metabolites, as described previously (*33*, *85*). Metabolites were washed with 4 ml of PBS for targeted steady-state samples and extracted on dry ice with 4 ml of 80% methanol (−80°C), as described previously (*86*–*88*). Insoluble material emerged as a pellet by centrifugation at 3000 RCF for 5 min, followed by two consecutive extractions of the insoluble pellet with 0.5 ml of 80% methanol, with centrifugation at 20,000 RCF for 5 min. The 5-ml metabolite extract from the pooled triplicate supernatants was dried under nitrogen gas using N-EVAP (Organomation Inc., Associates). Next, 50% acetonitrile (ACN) was added to the samples and vortexed for 30 s. Sample solutions were then

centrifuged at 20,000 RCF for 30 min at 4°C. The supernatant was collected for LC-MS analysis.

Spatially resolved multiomic analysis

Analysis was performed using the Freiburg Spatial Biology Database and the SPATAData package. Raw data are available at Datadryad. Data visualization was performed by the SPATA2::plotSurface() function. Expression values are denoised by an autoencoder implemented in SPATA2, and a bivariate kernel was applied for visualization. Spatially weighted correlation analysis was performed by Monte Carlo testing as follows: (1) estimation of the true correlation based on all spots; (2) a random selection of a permutation of the spots, preserving the spatial coordinates of the same parameters; (3) determination of a simulated correlation at all spots using randomized data from step 2; (4) repeating steps 2 and 3 100 times. At each spot, the rank of the one accurate correlation within the distribution of the simulated correlations was computed. The correlation must be in the upper or lower second 5% tail of the ranked distribution to be considered significant. The exact spatially weighted correlation was used for the co-correlation analysis of aligned metabolomic/transcriptomic data. The metabolites were selected using the MetaSpace database.

Hydrophilic metabolite profiling

For complete metabolomic profiling, samples were analyzed by high-performance liquid chromatography, high-resolution mass spectrometry, and tandem mass spectrometry (HPLC-MS/MS) (*33*). The system consisted of Thermo Q Exactive with an electrospray source and an Ultimate 3000 (Thermo Fisher Scientific) series HPLC consisting of a binary pump, degasser, and autosampler outfitted with an Xbridge Amide column (Waters; dimensions of 4.6 mm by 100 mm and a 3.5-mm particle size). Mobile phase A contained 95% (v/v) water, 5% (v/v) ACN, 20 mM ammonium hydroxide, and 20 mM ammonium acetate (pH 9.0); B was 100% ACN. The gradient was as follows: 0 min, 15% A; 2.5 min, 30% A; 7 min, 43% A; 16 min, 62% A; 16.1 to 18 min, 75% A; 18 to 25 min, 15% A, with a flow rate of 400 liters/min. The capillary of the electrospray ionization source was set to 275°C, with sheath gas at 45 arbitrary units, auxiliary gas at 5 arbitrary units, and the spray voltage at 4.0 kV. In positive/negative polarity switching mode, a mass/charge ratio (m/z) scan range from 70 to 850 was chosen, and MS1 data were collected at a resolution of 70,000. The automatic gain control target was set at 1×10^6, and the maximum injection time was 200 ms. The top five precursor ions were subsequently fragmented, in a data-dependent manner, using the higher-energy collisional dissociation cell set to 30% normalized collision energy in MS2 at a resolution power of 17,500. Data acquisition and analysis were performed using Xcalibur 4.1 software and TraceFinder 4.1 software, respectively (Thermo Fisher Scientific).

^{3}H-guanine and ^{3}H-uridine incorporation into DNA

The treated cells were labeled with 1 μCi of either ^{3}H-uridine or ^{3}H-guanine as previously described (*33*). First, cells were harvested, and DNA was isolated using AllPrep DNA/RNA kits according to the manufacturer's instructions and quantified using a spectrophotometer. Next, 70 μl of eluted DNA was added to scintillation vials, and radioactivity was measured by liquid scintillation counting and then normalized to the total DNA concentrations.

Statistics

Statistical analyses were performed and represented using GraphPad Prism v9.0 software (GraphPad Software, San Diego, CA, USA). Data are presented as mean with SD. Differences between the two groups were assessed using Student's t test or Wilcoxon rank sum test. Differences among multiple groups were evaluated using analysis of variance (ANOVA) with post hoc Tukey's or Mann-Whitney U tests with Bonferroni correction. In vivo survival curves were graphed with the Kaplan-Meier method and compared using the log-rank test. All tests were two-sided with $P < 0.05$. In vitro experiments like flow cytometry, cell viability assays, isotope tracing, and metabolomic experiments were performed in biological triplicates.

Supplementary Materials

This PDF file includes:

Figs. S1 to S10

REFERENCES AND NOTES

1. M. Greaves, C. C. Maley, Clonal evolution in cancer. *Nature* **481**, 306–313 (2012).
2. K. S. Korolev, J. B. Xavier, J. Gore, Turning ecology and evolution against cancer. *Nat. Rev. Cancer* **14**, 371–380 (2014).
3. P. C. Nowell, The clonal evolution of tumor cell populations: Acquired genetic lability permits stepwise selection of variant sublines and underlies tumor progression. *Science* **194**, 23–28 (1976).
4. F. Thomas, D. Fisher, P. Fort, J. P. Marie, S. Daoust, B. Roche, C. Grunau, C. Cosseau, G. Mitta, S. Baghdiguian, F. Rousset, P. Lassus, E. Assenat, D. Grégoire, D. Missé, A. Lorz, F. Billy, W. Vainchenker, F. Delhommeau, S. Koscielny, R. Itzykson, R. Tang, F. Fava, A. Ballesta, T. Lepoutre, L. Krasinska, V. Dulic, P. Raynaud, P. Blache, C. Quittau-Prevostel, E. Vignal, H. Trauchessec, B. Perthame, J. Clairambault, V. Volpert, E. Solary, U. Hibner, M. E. Hochberg, Applying ecological and evolutionary theory to cancer: A long and winding road. *Evol. Appl.* **6**, 1–10 (2013).
5. R. E. Stace, T. Stiehl, M. A. Chaplain, A. Marciniak-Czochra, T. Lorenzi, Discrete and continuum phenotype-structured models for the evolution of cancer cell populations under chemotherapy. *Math. Model. Nat. Phenom.* **15**, 14 (2020).
6. R. H. Chisholm, T. Lorenzi, A. Lorz, A. K. Larsen, L. N. Almeida, A. Escargueil, J. Clairambault, Emergence of drug tolerance in cancer cell populations: An evolutionary outcome of selection, nongenetic instability, and stress-induced adaptation. *Cancer Res.* **75**, 930–939 (2015).
7. H. Cho, D. Levy, Modeling the chemotherapy-induced selection of drug-resistant traits during tumor growth. *J. Theor. Biol.* **436**, 120–134 (2018).
8. T. Lorenzi, R. H. Chisholm, J. Clairambault, Tracking the evolution of cancer cell populations through the mathematical lens of phenotype-structured equations. *Biol. Direct* **11**, 1–17 (2016).
9. I. Olmez, W. Shen, H. McDonald, B. Ozpolat, Dedifferentiation of patient-derived glioblastoma multiforme cell lines results in a cancer stem cell-like state with mitogen-independent growth. *J. Cell. Mol. Med.* **19**, 1262–1272 (2015).
10. A. R. Safa, M. R. Saadatzadeh, A. A. Cohen-Gadol, K. E. Pollok, K. Bijangi-Vishehsaraei, Glioblastoma stem cells (GSCs) epigenetic plasticity and interconversion between differentiated non-GSCs and GSCs. *Genes Dis.* **2**, 152–163 (2015).
11. B. Auffinger, A. L. Tobias, Y. Han, G. Lee, D. Guo, M. Dey, M. S. Lesniak, A. U. Ahmed, Conversion of differentiated cancer cells into cancer stem-like cells in a glioblastoma model after primary chemotherapy. *Cell Death Differ.* **21**, 1119–1131 (2014).
12. C. L. Chaffer, I. Brueckmann, C. Scheel, A. J. Kaestli, P. A. Wiggins, L. O. Rodrigues, M. Brooks, F. Reinhardt, Y. Su, K. Polyak, L. M. Arendt, C. Kuperwasser, B. Bierie, R. A. Weinberg, Normal and neoplastic nonstem cells can spontaneously convert to a stem-like state. *Proc. Natl. Acad. Sci. U.S.A.* **108**, 7950–7955 (2011).
13. Y. Tamori, W.-M. Deng, Cell competition and its implications for development and cancer. *J. Genet. Genomics* **38**, 483–495 (2011).
14. A. Lorz, T. Lorenzi, M. E. Hochberg, J. Clairambault, B. Perthame, Populational adaptive evolution, chemotherapeutic resistance and multiple anti-cancer therapies. *ESAIM Math. Model. Numer. Anal.* **47**, 377–399 (2013).
15. S. Osuka, E. G. Van Meir, Overcoming therapeutic resistance in glioblastoma: The way forward. *J. Clin. Invest.* **127**, 415–426 (2017).

16. Y. P. Ramirez, J. L. Weatherbee, R. T. Wheelhouse, A. H. Ross, Glioblastoma multiforme therapy and mechanisms of resistance. *Pharmaceuticals* **6**, 1475–1506 (2013).
17. J. W. Fairman, S. R. Wijerathna, M. F. Ahmad, H. Xu, R. Nakano, S. Jha, J. Prendergast, R. M. Welin, S. Flodin, A. Roos, P. Nordlund, Z. Li, T. Walz, C. G. Dealwis, Structural basis for allosteric regulation of human ribonucleotide reductase by nucleotide-induced oligomerization. *Nat. Struct. Mol. Biol.* **18**, 316–322 (2011).
18. A. Miah, K. Harrington, C. Nutting, Triapine in clinical practice. *Eur. J. Clin. Med. Oncol.* **2**, 1 (2010).
19. G. L. Manno, R. Soldatov, A. Zeisel, E. Braun, H. Hochgerner, V. Petukhov, K. Lidschreiber, M. E. Kastriti, P. Lönnerberg, A. Furlan, J. Fan, L. E. Borm, Z. Liu, D. van Bruggen, J. Guo, X. He, R. Barker, E. Sundström, G. Castelo-Branco, P. Cramer, I. Adameyko, S. Linnarsson, P. V. Kharchenko, RNA velocity of single cells. *Nature* **560**, 494–498 (2018).
20. R. Bazzoni, A. Bentivegna, Role of notch signaling pathway in glioblastoma pathogenesis. *Cancer* **11**, 292 (2019).
21. K. E. Hovinga, F. Shimizu, R. Wang, G. Panagiotakos, M. van der Heijden, H. Moayedpardazi, A. S. Correia, D. Soulet, T. Major, J. Menon, V. Tabar, Inhibition of notch signaling in glioblastoma targets cancer stem cells via an endothelial cell intermediate. *Stem Cells* **28**, 1019–1029 (2010).
22. M.-T. Stockhausen, K. Kristoffersen, H. S. Poulsen, The functional role of Notch signaling in human gliomas. *Neuro Oncol.* **12**, 199–211 (2010).
23. K. Van den Berge, H. R. de Bézieux, K. Street, W. Saelens, R. Cannoodt, Y. Saeys, S. Dudoit, L. Clement, Trajectory-based differential expression analysis for single-cell sequencing data. *Nat. Commun.* **11**, 1–13 (2020).
24. K. R. Campbell, C. Yau, Uncovering pseudotemporal trajectories with covariates from single cell and bulk expression data. *Nat. Commun.* **9**, 1–12 (2018).
25. R. G. Verhaak, K. A. Hoadley, E. Purdom, V. Wang, Y. Qi, M. D. Wilkerson, C. R. Miller, L. Ding, T. Golub, J. P. Mesirov, G. Alexe, M. Lawrence, M. O'Kelly, P. Tamayo, B. A. Weir, S. Gabriel, W. Winckler, S. Gupta, L. Jakkula, H. S. Feiler, J. G. Hodgson, C. D. James, J. N. Sarkaria, C. Brennan, A. Kahn, P. T. Spellman, R. K. Wilson, T. P. Speed, J. W. Gray, M. Meyerson, G. Getz, C. M. Perou, D. N. Hayes; Cancer Genome Atlas Research Network, Integrated genomic analysis identifies clinically relevant subtypes of glioblastoma characterized by abnormalities in PDGFRA, IDH1, EGFR, and NF1. *Cancer Cell* **17**, 98–110 (2010).
26. C. Neftel, J. Laffy, M. G. Filbin, T. Hara, M. E. Shore, G. J. Rahme, A. R. Richman, D. Silverbush, M. K. L. Shaw, C. M. Hebert, J. Dewitt, S. Gritsch, E. M. Perez, L. N. Gonzalez Castro, X. Lan, N. Druck, C. Rodman, D. Dionne, A. Kaplan, M. S. Bertalan, J. Small, K. Pelton, S. Becker, D. Bonal, Q. D. Nguyen, R. L. Servis, J. M. Fung, R. Mylvaganam, L. Mayr, J. Gojo, C. Haberler, R. Geyeregger, T. Czech, I. Slavc, B. V. Nahed, W. T. Curry, B. S. Carter, H. Wakimoto, P. K. Brastianos, T. T. Batchelor, A. Stemmer-Rachamimov, M. Martinez-Lage, M. P. Frosch, I. Stamenkovic, N. Riggi, E. Rheinbay, M. Monje, O. Rozenblatt-Rosen, D. P. Cahill, A. P. Patel, T. Hunter, I. M. Verma, K. L. Ligon, D. N. Louis, A. Regev, B. E. Bernstein, I. Tirosh, M. L. Suvà, An integrative model of cellular states, plasticity, and genetics for glioblastoma. *Cell* **178**, 835–849.e21 (2019).
27. A. P. Patel, I. Tirosh, J. J. Trombetta, A. K. Shalek, S. M. Gillespie, H. Wakimoto, D. P. Cahill, B. V. Nahed, W. T. Curry, R. L. Martuza, D. N. Louis, O. Rozenblatt-Rosen, M. L. Suvà, A. Regev, B. E. Bernstein, Single-cell RNA-seq highlights intratumoral heterogeneity in primary glioblastoma. *Science* **344**, 1396–1401 (2014).
28. Q. Wang, B. Hu, X. Hu, H. Kim, M. Squatrito, L. Scarpace, A. C. deCarvalho, S. Lyu, P. Li, Y. Li, F. Barthel, H. J. Cho, Y. H. Lin, N. Satani, E. Martinez-Ledesma, S. Zheng, E. Chang, C. E. G. Sauvé, A. Olar, Z. D. Lan, G. Finocchiaro, J. J. Phillips, M. S. Berger, K. R. Gabrusiewicz, G. Wang, E. Eskilsson, J. Hu, T. Mikkelsen, R. A. DePinho, F. Muller, A. B. Heimberger, E. P. Sulman, D. H. Nam, R. G. W. Verhaak, Tumor evolution of glioma-intrinsic gene expression subtypes associates with immunological changes in the microenvironment. *Cancer Cell* **32**, 42–56.e6 (2017).
29. S. Maniatis, J. Petrescu, H. Phatnani, Spatially resolved transcriptomics and its applications in cancer. *Curr. Opin. Genet. Dev.* **66**, 70–77 (2021).
30. V. M. Ravi, P. Will, J. Kueckelhaus, N. Sun, K. Joseph, H. Salié, L. Vollmer, U. Kuliesiute, J. von Ehr, J. K. Benotmane, N. Neidert, M. Follo, F. Scherer, J. M. Goeldner, S. P. Behringer, P. Franco, M. Khiat, J. Zhang, U. G. Hofmann, C. Fung, F. L. Ricklefs, K. Lamszus, M. Boerries, M. Ku, J. Beck, R. Sankowski, M. Schwabenland, M. Prinz, U. Schüller, S. Killmer, B. Bengsch, A. K. Walch, D. Delev, O. Schnell, D. H. Heiland, Spatially resolved multi-omics deciphers bidirectional tumor-host interdependence in glioblastoma. *Cancer Cell* **40**, 639–655.e13 (2022).
31. L. P. Serwer, C. O. Noble, K. Michaud, D. C. Drummond, D. B. Kirpotin, T. Ozawa, M. D. Prados, J. W. Park, C. D. James, Investigation of intravenous delivery of nanoliposomal topotecan for activity against orthotopic glioblastoma xenografts. *Neuro Oncol.* **13**, 1288–1295 (2011).
32. A. Bhaduri, E. di Lullo, D. Jung, S. Müller, E. E. Crouch, C. S. Espinosa, T. Ozawa, B. Alvarado, J. Spatazza, C. R. Cadwell, G. Wilkins, D. Velmeshev, S. J. Liu, M. Malatesta, M. G. Andrews, M. A. Mostajo-Radji, E. J. Huang, T. J. Nowakowski, D. A. Lim, A. Diaz, D. R. Raleigh, A. R. Kriegstein, Outer radial glia-like cancer stem cells contribute to heterogeneity of glioblastoma. *Cell Stem Cell* **26**, 48–63.e6 (2020).
33. J. M. Shireman, F. Atashi, G. Lee, E. S. Ali, M. R. Saathoff, C. H. Park, S. Savchuk, S. Baisiwala, J. Miska, M. S. Lesniak, C. D. James, R. Stupp, P. Kumthekar, C. M. Horbinski, I. Ben-Sahra, A. U. Ahmed, De novo purine biosynthesis is a major driver of chemoresistance in glioblastoma. *Brain* **144**, 1230–1246 (2021).
34. K. Hyun, J. Jeon, K. Park, J. Kim, Writing, erasing and reading histone lysine methylations. *Exp. Mol. Med.* **49**, e324 (2017).
35. I. P. Foskolou, C. Jorgensen, K. B. Leszczynska, M. M. Olcina, H. Tarhonskaya, B. Haisma, V. D'Angiolella, W. K. Myers, C. Domene, E. Flashman, E. M. Hammond, Ribonucleotide reductase requires subunit switching in hypoxia to maintain DNA replication. *Mol. Cell* **66**, 206–220. e9 (2017).
36. R. N. Curry, S. M. Glasgow, The Role of neurodevelopmental pathways in brain tumors. *Front. Cell Dev. Biol.* **9**, 659055 (2021).
37. M. G. Filbin, S. K. Dabral, M. F. Pazyra-Murphy, S. Ramkissoon, A. L. Kung, E. Pak, J. Chung, M. A. Theisen, Y. Sun, Y. Franchetti, Y. Sun, D. S. Shulman, N. Redjal, B. Tabak, R. Beroukhim, Q. Wang, J. Zhao, M. Dorsch, S. Buonamici, K. L. Ligon, J. F. Kelleher, R. A. Segal, Coordinate activation of Shh and PI3K signaling in PTEN-deficient glioblastoma: New therapeutic opportunities. *Nat. Med.* **19**, 1518–1523 (2013).
38. T. Chakkath, S. Lavergne, T. M. Fan, D. Bunick, L. Dirikolu, Alkylation and carbamylation effects of lomustine and its major metabolites and MGMT expression in canine cells. *Vet. Sci.* **2**, 52–68 (2015).
39. A. Tsubura, K. Yoshizawa, T. Sasaki, in *Encyclopedia of Toxicology (Third Edition)*, P. Wexler, Ed. (Academic Press, 2014), pp. 321–323.
40. A. D. Thomas, G. E. Johnson, in *Thresholds of Genotoxic Carcinogens,* T. Nohmi, S. Fukushima, Eds. (Academic Press, 2016), pp. 67–82.
41. B. Auffinger, D. Spencer, P. Pytel, A. U. Ahmed, M. S. Lesniak, The role of glioma stem cells in chemotherapy resistance and glioblastoma multiforme recurrence. *Expert Rev. Neurother.* **15**, 741–752 (2015).
42. S. Baisiwala, R. R. Hall III, M. R. Saathoff, J. M. Shireman, C. Park, S. Budhiraja, C. Goel, L. Warnke, C. Hardiman, J. Y. Wang, K. McCortney, C. M. Horbinski, A. U. Ahmed, LNX1 modulates Notch1 signaling to promote expansion of the glioma stem cell population during temozolomide therapy in glioblastoma. *Cancer* **12**, 3505 (2020).
43. R. A. Finch, M. C. Liu, S. P. Grill, W. C. Rose, R. Loomis, K. M. Vasquez, Y. C. Cheng, A. C. Sartorelli, Triapine (3-aminopyridine-2-carboxaldehyde-thiosemicarbazone): A potent inhibitor of ribonucleotide reductase activity with broad spectrum antitumor activity. *Biochem. Pharmacol.* **59**, 983–991 (2000).
44. M. McCord, E. Bartom, K. Burdett, A. Baran, F. D. Eckerdt, I. V. Balyasnikova, K. McCortney, T. Sears, S. Y. Cheng, J. N. Sarkaria, R. Stupp, A. B. Heimberger, A. Ahmed, C. D. James, C. Horbinski, Modeling therapy-driven evolution of glioblastoma with patient-derived xenografts. *Cancers (Basel)* **14**, 5494 (2022).
45. E. Villa, E. S. Ali, U. Sahu, I. Ben-Sahra, Cancer cells tune the signaling pathways to empower de novo synthesis of nucleotides. *Cancers (Basel)* **11**, 688 (2019).
46. N. Zarco, E. Norton, A. Quiñones-Hinojosa, H. Guerrero-Cázares, Overlapping migratory mechanisms between neural progenitor cells and brain tumor stem cells. *Cell. Mol. Life Sci.* **76**, 3553–3570 (2019).
47. H. Playa, T. A. Lewis, A. Ting, B. C. Suh, B. Muñoz, R. Matuza, B. J. Passer, S. L. Schreiber, J. K. Buolamwini, Dilazep analogues for the study of equilibrative nucleoside transporters 1 and 2 (ENT1 and ENT2). *Bioorg. Med. Chem. Lett.* **24**, 5801–5804 (2014).
48. H. Easwaran, H.-C. Tsai, S. B. Baylin, Cancer epigenetics: Tumor heterogeneity, plasticity of stem-like states, and drug resistance. *Mol. Cell* **54**, 716–727 (2014).
49. J. Chen, Y. Li, T. S. Yu, R. M. McKay, D. K. Burns, S. G. Kernie, L. F. Parada, A restricted cell population propagates glioblastoma growth after chemotherapy. *Nature* **488**, 522–526 (2012).
50. L. Oliver, L. Lalier, C. Salaud, D. Heymann, P. F. Cartron, F. M. Vallette, Drug resistance in glioblastoma: Are persisters the key to therapy? *Cancer Drug Resist.* **3**, 287–301 (2020).
51. C. Darwin, *On the Origin of Species by Means of Natural Selection or the Preservation of Favoured Races in the Struggle for Life* (Books, Incorporated, 1859), vol. 2.
52. Z. Yu, T. G. Pestell, M. P. Lisanti, R. G. Pestell, Cancer stem cells. *Int. J. Biochem. Cell Biol.* **44**, 2144–2151 (2012).
53. A. L. V. Alves, I. N. F. Gomes, A. C. Carloni, M. N. Rosa, L. S. da Silva, A. F. Evangelista, R. M. Reis, V. A. O. Silva, Role of glioblastoma stem cells in cancer therapeutic resistance: A perspective on antineoplastic agents from natural sources and chemical derivatives. *Stem Cell Res. Ther.* **12**, 1–22 (2021).
54. H. Erasimus, M. Gobin, S. Niclou, E. Van Dyck, DNA repair mechanisms and their clinical impact in glioblastoma. *Mutat. Res./Rev. Mutat. Res.* **769**, 19–35 (2016).
55. P. S. Mischel, R. Shai, T. Shi, S. Horvath, K. V. Lu, G. Choe, D. Seligson, T. J. Kremen, A. Palotie, L. M. Liau, T. F. Cloughesy, S. F. Nelson, Identification of molecular subtypes of glioblastoma by gene expression profiling. *Oncogene* **22**, 2361–2373 (2003).

56. J. Briscoe, B. G. Novitch, Regulatory pathways linking progenitor patterning, cell fates and neurogenesis in the ventral neural tube. *Philos. Trans. R Soc. B Biol. Sci.* **363**, 57–70 (2008).
57. J. Behnan, G. Finocchiaro, G. Hanna, The landscape of the mesenchymal signature in brain tumours. *Brain* **142**, 847–866 (2019).
58. B. Yousefi, M. Rahmati, Y. Ahmadi, The roles of p53R2 in cancer progression based on the new function of mutant p53 and cytoplasmic p21. *Life Sci.* **99**, 14–17 (2014).
59. H. Tanaka, H. Arakawa, T. Yamaguchi, K. Shiraishi, S. Fukuda, K. Matsui, Y. Takei, Y. Nakamura, A ribonucleotide reductase gene involved in a p53-dependent cell-cycle checkpoint for DNA damage. *Nature* **404**, 42–49 (2000).
60. X. Liu, L. Xue, Y. Yen, *Advanced Protocols in Oxidative Stress I* (Springer, 2008), pp. 195–206.
61. N. Rohatgi, U. Ghoshdastider, P. Baruah, T. Kulshrestha, A. J. Skanderup, A pan-cancer metabolic atlas of the tumor microenvironment. *Cell Rep.* **39**, 110800 (2022).
62. S. K. Singh, I. D. Clarke, M. Terasaki, V. E. Bonn, C. Hawkins, J. Squire, P. B. Dirks, Identification of a cancer stem cell in human brain tumors. *Cancer Res.* **63**, 5821–5828 (2003).
63. S. Bao, Q. Wu, R. E. McLendon, Y. Hao, Q. Shi, A. B. Hjelmeland, M. W. Dewhirst, D. D. Bigner, J. N. Rich, Glioma stem cells promote radioresistance by preferential activation of the DNA damage response. *Nature* **444**, 756–760 (2006).
64. A.-M. Bleau, D. Hambardzumyan, T. Ozawa, E. I. Fomchenko, J. T. Huse, C. W. Brennan, E. C. Holland, PTEN/PI3K/Akt pathway regulates the side population phenotype and ABCG2 activity in glioma tumor stem-like cells. *Cell Stem Cell* **4**, 226–235 (2009).
65. S. R. C. Immanuel, A. D. Ghanate, D. S. Parmar, R. Yadav, R. Uthup, V. Panchagnula, A. Raghunathan, Integrated genetic and metabolic landscapes predict vulnerabilities of temozolomide resistant glioblastoma cells. *NPJ Syst. Biol. Appl.* **7**, 1–10 (2021).
66. A. Chabes, B. Georgieva, V. Domkin, X. Zhao, R. Rothstein, L. Thelander, Survival of DNA damage in yeast directly depends on increased dNTP levels allowed by relaxed feedback inhibition of ribonucleotide reductase. *Cell* **112**, 391–401 (2003).
67. C. W. Brennan, R. G. W. Verhaak, A. McKenna, B. Campos, H. Noushmehr, S. R. Salama, S. Zheng, D. Chakravarty, J. Z. Sanborn, S. H. Berman, R. Beroukhim, B. Bernard, C. J. Wu, G. Genovese, I. Shmulevich, J. Barnholtz-Sloan, L. Zou, R. Vegesna, S. A. Shukla, G. Ciriello, W. K. Yung, W. Zhang, C. Sougnez, T. Mikkelsen, K. Aldape, D. D. Bigner, E. G. van Meir, M. Prados, A. Sloan, K. L. Black, J. Eschbacher, G. Finocchiaro, W. Friedman, D. W. Andrews, A. Guha, M. Iacocca, B. P. O'Neill, G. Foltz, J. Myers, D. J. Weisenberger, R. Penny, R. Kucherlapati, C. M. Perou, D. N. Hayes, R. Gibbs, M. Marra, G. B. Mills, E. Lander, P. Spellman, R. Wilson, C. Sander, J. Weinstein, M. Meyerson, S. Gabriel, P. W. Laird, D. Haussler, G. Getz, L. Chin; on behalf of the TCGA Research Network, The somatic genomic landscape of glioblastoma. *Cell* **155**, 462–477 (2013).
68. R. D. Rasmussen, M. K. Gajjar, L. Tuckova, K. E. Jensen, A. Maya-Mendoza, C. B. Holst, K. Møllgaard, J. S. Rasmussen, J. Brennum, J. Bartek Jr., M. Syrucek, E. Sedlakova, K. K. Andersen, M. H. Frederiksen, J. Bartek, P. Hamerlik, BRCA1-regulated RRM2 expression protects glioblastoma cells from endogenous replication stress and promotes tumorigenicity. *Nat. Commun.* **7**, 13398 (2016).
69. J. Gojo, B. Englinger, L. Jiang, J. M. Hübner, M. K. L. Shaw, O. A. Hack, S. Madlener, D. Kirchhofer, I. Liu, J. Pyrdol, V. Hovestadt, E. Mazzola, N. D. Mathewson, M. Trissal, D. Lötsch, C. Dorfer, C. Haberler, A. Halfmann, L. Mayr, A. Peyrl, R. Geyeregger, B. Schwalm, M. Mauermann, K. W. Pajtler, T. Milde, M. E. Shore, J. E. Geduldig, K. Pelton, T. Czech, O. Ashenberg, K. W. Wucherpfennig, O. Rozenblatt-Rosen, S. Alexandrescu, K. L. Ligon, S. M. Pfister, A. Regev, I. Slavc, W. Berger, M. L. Suvà, M. Kool, M. G. Filbin, Single-cell RNA-seq reveals cellular hierarchies and impaired developmental trajectories in pediatric ependymoma. *Cancer Cell* **38**, 44–59.e9 (2020).
70. S. J. Baker, D. W. Ellison, D. H. Gutmann, Pediatric gliomas as neurodevelopmental disorders. *Glia* **64**, 879–895 (2016).
71. E. Crespan, A. Garbelli, A. Amoroso, G. Maga, Exploiting the nucleotide substrate specificity of repair DNA polymerases to develop novel anticancer agents. *Molecules* **16**, 7994–8019 (2011).
72. F. T. Merkle, A. D. Tramontin, J. M. García-Verdugo, A. Alvarez-Buylla, Radial glia give rise to adult neural stem cells in the subventricular zone. *Proc. Natl. Acad. Sci. U.S.A.* **101**, 17528–17532 (2004).
73. C. P. Couturier, S. Ayyadhury, P. U. Le, J. Nadaf, J. Monlong, G. Riva, R. Allache, S. Baig, X. Yan, M. Bourgey, C. Lee, Y. C. D. Wang, V. W. Yong, M.-C. Guiot, H. Najafabadi, B. Misic, J. Antel, G. Bourque, J. Ragoussis, K. Petrecca, Single-cell RNA-seq reveals that glioblastoma recapitulates a normal neurodevelopmental hierarchy. *Nat. Commun.* **11**, 1–19 (2020).
74. S. Baisiwala, B. Auffinger, S. P. Caragher, J. M. Shireman, R. Ahsan, G. Lee, T. Hasan, C. Park, M. R. Saathoff, A. C. Christensen, A. U. Ahmed, Chemotherapeutic stress induces transdifferentiation of glioblastoma cells to endothelial cells and promotes vascular mimicry. *Stem Cells Int.* **2019**, 1–14 (2019).
75. E. Z. Macosko, A. Basu, R. Satija, J. Nemesh, K. Shekhar, M. Goldman, I. Tirosh, A. R. Bialas, N. Kamitaki, E. M. Martersteck, J. J. Trombetta, D. A. Weitz, J. R. Sanes, A. K. Shalek, A. Regev, S. A. McCarroll, Highly parallel genome-wide expression profiling of individual cells using nanoliter droplets. *Cell* **161**, 1202–1214 (2015).
76. T. Stuart, A. Butler, P. Hoffman, C. Hafemeister, E. Papalexi, W. M. Mauck III, Y. Hao, M. Stoeckius, P. Smibert, R. Satija, Comprehensive integration of single-cell data. *Cell* **177**, 1888–1902.e21 (2019).
77. Aselewa. (github, 2019). https://github.com/aselewa/dropseqRunner.
78. Y. Hao, S. Hao, E. Andersen-Nissen, W. M. Mauck, 3rd, S. Zheng, A. Butler, M. J. Lee, A. J. Wilk, C. Darby, M. Zager, P. Hoffman, M. Stoeckius, E. Papalexi, E. P. Mimitou, J. Jain, A. Srivastava, T. Stuart, L. M. Fleming, B. Yeung, A. J. Rogers, J. M. McElrath, C. A. Blish, R. Gottardo, P. Smibert, R. Satija, Integrated analysis of multimodal single-cell data. *Cell* **184**, 3573–3587.e29 (2021).
79. I. Sharma, A. Singh, F. Siraj, S. Saxena, IL-8/CXCR1/2 signalling promotes tumor cell proliferation, invasion and vascular mimicry in glioblastoma. *J. Biomed. Sci.* **25**, 1–13 (2018).
80. H. Li, L. Chen, J.-J. Li, Q. Zhou, A. Huang, W.-W. Liu, K. Wang, L. Gao, S.-T. Qi, Y.-T. Lu, miR-519a enhances chemosensitivity and promotes autophagy in glioblastoma by targeting STAT3/Bcl2 signaling pathway. *J. Hematol. Oncol.* **11**, 1–16 (2018).
81. G. Tiscornia, O. Singer, I. M. Verma, Production and purification of lentiviral vectors. *Nat. Protoc.* **1**, 241–245 (2006).
82. J. Elegheert, E. Behiels, B. Bishop, S. Scott, R. E. Woolley, S. C. Griffiths, E. F. X. Byrne, V. T. Chang, D. I. Stuart, E. Y. Jones, C. Siebold, A. R. Aricescu, Lentiviral transduction of mammalian cells for fast, scalable and high-level production of soluble and membrane proteins. *Nat. Protoc.* **13**, 2991–3017 (2018).
83. T. Hasan, S. P. Caragher, J. M. Shireman, C. H. Park, F. Atashi, S. Baisiwala, G. Lee, D. Guo, J. Y. Wang, M. Dey, M. Wu, M. S. Lesniak, C. M. Horbinski, C. D. James, A. U. Ahmed, Interleukin-8/CXCR2 signaling regulates therapy-induced plasticity and enhances tumorigenicity in glioblastoma. *Cell Death Dis.* **10**, 1–17 (2019).
84. H. Iqbal, D. R. Akins, M. R. Kenedy, *Borrelia Burgdorferi* (Springer, 2018), pp. 47–55.
85. I. Ben-Sahra, J. J. Howell, J. M. Asara, B. D. Manning, Stimulation of de novo pyrimidine synthesis by growth signaling through mTOR and S6K1. *Science* **339**, 1323–1328 (2013).
86. D. N. Weinberg, S. Papillon-Cavanagh, H. Chen, Y. Yue, X. Chen, K. N. Rajagopalan, C. Horth, J. T. McGuire, X. Xu, H. Nikbakht, A. E. Lemiesz, D. M. Marchione, M. R. Marunde, M. J. Meiners, M. A. Cheek, M. C. Keogh, E. Bareke, A. Djedid, A. S. Harutyunyan, N. Jabado, B. A. Garcia, H. Li, C. D. Allis, J. Majewski, C. Lu, The histone mark H3K36me2 recruits DNMT3A and shapes the intergenic DNA methylation landscape. *Nature* **573**, 281–286 (2019).
87. M. Yuan, S. B. Breitkopf, X. Yang, J. M. Asara, A positive/negative ion–switching, targeted mass spectrometry–based metabolomics platform for bodily fluids, cells, and fresh and fixed tissue. *Nat. Protoc.* **7**, 872–881 (2012).
88. E. S. Ali, U. Sahu, E. Villa, B. P. O'Hara, P. Gao, C. Beaudet, A. W. Wood, J. M. Asara, I. Ben-Sahra, ERK2 phosphorylates PFAS to mediate posttranslational control of de novo purine synthesis. *Mol. Cell* **78**, 1178–1191.e6 (2020).

Acknowledgments: The work in this manuscript is dedicated to the memory of J. Nordell. We thank J. Talton and nanopharmaceuticals for providing us with the clinical-grade second-generation RRM2 inhibitor 3-AP. **Funding:** The National Institute of Neurological Disorders and Stroke supported this work with grants 1R01NS096376, 1R01NS112856, and P50CA221747 SPORE for Translational Approaches to Brain Cancer (to A.U.A.), R01GM135587, and R01GM143334 (to I.B.-S.). This work was partly supported by the Else Kröner-Fresenius Foundation and MEPHISTO project BMBF (Germany Ministry of Education and Research, project number 031L0260B) (to D.H.H.). **Author contributions:** Conceptualization: E.N.P., J.M.S., and A.U.A. Methodology: E.N.P., J.M.S., E.S.A., J.M., and A.U.A. Validation, formal analysis, and investigation: E.N.P., E.S.A., I.P., P.L., D.H.H., C.P., S.Bu., and S.Ba. Resources: A.U.A., D.H.H., I.B.-S., C.D.J., S.P., A.B., and J.M. Data curation and draft preparation: E.N.P., P.L., I.P., and D.H.H. Review and editing: E.N.P., J.M.S., E.S.A., I.P., S.Bu., K.D., C.D.J., D.H.H., I.B.-S., S.P., A.B., J.M., and A.U.A. Supervision, project administration, and funding acquisition: A.U.A. **Competing interests:** The authors declare that they have no competing interest. **Data and materials availability:** The results published here are in part based on data generated by the TCGA Research Network (www.cancer.gov/tcga) and were further analyzed through GlioVis. In addition, these results use data generated by the Human Protein Atlas and GBMSeq (Gephart Laboratory, www.gbmseq.org). Figures, in part, were generated using BioRender (www.biorender.com). All relevant sequencing files were deposited into the GEO repository, accession number: GSE227348. All data needed to evaluate the conclusions in the paper are present in the paper and/or the Supplementary Materials.

Submitted 3 September 2022
Accepted 13 April 2023
Published 17 May 2023
10.1126/sciadv.ade7236